2420-9-P

AD705228

INVESTIGATION OF HOLOGRAPHIC TESTING TECHNIQUES

Semiannual Report

1 June Through 30 November 1969

E. N. LEITH
C. M. VEST

April 1970

UNIVERSITY OF MICHIGAN
1817

RADAR AND OPTICS LABORATORY
Willow Run Laboratories
INSTITUTE OF SCIENCE AND TECHNOLOGY

Prepared for the Advanced Research Projects Agency, Department of Defense, Washington, D. C., ARPA Order No. 1245, Program Code No. 8D10, Contract No. DAAG46-69-C-0017

DDC
RECEIVED
MAY 6 1970
C

18

2420-9-P

INVESTIGATION OF HOLOGRAPHIC TESTING TECHNIQUES

Semiannual Report

1 June Through 30 November 1969

E. N. LEITH
C. M. VEST

April 1970

Radar and Optics Laboratory
Willow Run Laboratories
INSTITUTE OF SCIENCE AND TECHNOLOGY
THE UNIVERSITY OF MICHIGAN
Ann Arbor, Michigan

FOREWORD

This report was prepared by the Radar and Optics Laboratory of the Willow Run Laboratories, a unit of The University of Michigan's Institute of Science and Technology, in conjunction with the Cooley Electronics Laboratory, under ARPA-sponsored NDT Research Contract DAAG46-69-C-0017 which began 1 December 1968. This report covers the work performed between 1 June 1969 and 30 November 1969. The contract is monitored by Mr. Robert C. Grubinskas, Nondestructive Testing Branch, Army Materials and Mechanics Research Center, Watertown, Massachusetts.

The investigation of modulated reference-beam holography and the work on variable sensitivity holographic interferometry was jointly sponsored by the Air Force under Contracts F33(615)-67-C-1814 and AF33(615)-68-C-1310.

The Principal Investigators on this project are C. M. Vest and E. N. Leith. Sections 2, 3, and 6 and Appendix I were contributed by D. W. Sweeney and C. M. Vest. Sections 4 and 5 and Appendix II were contributed by J. R. Varner, and Section 7 was contributed by C. C. Aleksoff. In Section 8, L. W. Orr reports the work conducted at the Cooley Electronics Laboratory of The University of Michigan. This work was submitted by the authors on 24 November 1969. The Willow Run Laboratories' number for this report is 2460-9-P.

ABSTRACT

This second semiannual report includes studies of interferometric detection of stress corrosion cracking, testing of honeycomb sandwich structures, techniques developed for pulsed-laser contouring and interferometry, laser speckle reduction in interferometry, modulated reference-wave holography, and flaw detection.

Holographic interferometry has been used to detect initiation of stress corrosion, monitor the progression of delayed cracking, and detect bond defects in an aircraft trim tab of honeycomb structure.

The several theoretical and experimental investigations conducted include the development of multiple-wavelength holographic interferometry, the study of techniques for improving interferometry of three-dimensional transparent objects, the application of modulated reference-wave holography to vibrating diffusely reflecting objects, and the application of hologram interferometry to detection of flaws in cylindrical steel objects.

BLANK PAGE

CONTENTS

Foreword iii

Abstract v

List of Figures ix

List of Tables x

1. Introduction 1

2. Monitoring of Stress Corrosion Cracking 2
    2.1. Background 2
        2.1.1. Detection of Microcracks 2
        2.1.2. Stress Cracking of Uranium Alloys 2
        2.1.3. Stress Corrosion Cracking of Titanium Alloys 3
    2.2. Holographic Interferometry 3
    2.3. Experimental Apparatus 5
        2.3.1. Optical Apparatus 5
        2.3.2. Test Specimen and Related Equipment 5
    2.4. Experimental Procedure 7
    2.5. Experimental Results 10
    2.6. Conclusions 11

3. Holographic Testing of Honeycomb Sandwich Aircraft Structure 17
    3.1. Introduction 17
    3.2. Experimental Apparatus and Procedure 17
    3.3. Experimental Results 19

4. Pulsed-Laser Holography 25
    4.1. Introduction 25
    4.2. Multiple-Wavelength Holographic Interferometry 25
        4.2.1. Pulsed-Laser Holographic Contouring 25
        4.2.2. Automatic Reference-Beam Compensation 25
        4.2.3. Nonlinear Recording 26

5. Variable Sensitivity Holographic Interferometry 29
    5.1. Introduction 29
    5.2. Theory 29
    5.3. Experimental Results 32
    5.4. Conclusions 35

6. Interferometry of Three-Dimensional Transparent Objects 36
    6.1. Introduction 36
    6.2. Possible Improvement of Fringe Visibility and Resolution 36
    6.3. Multidirectional Illumination 37

7. Modulated Reference-Wave Holography 38

8. Flaw Detection by Hologram Interferometry 41
    8.1. Introduction 41
    8.2. Pneumatic Technique 41
    8.3. Thermal Technique 46
    8.4. Compression Technique 46
    8.5. Vibration Technique 50

9. Ultrasonic Holography 54
Appendix I: Stress Corrosion Cracking of Titanium Alloys 55
Appendix II: Theory of Automatic Reference Beam Compensation 57
References 61
Distribution List 63

FIGURES

1. Optical Arrangement for Stress Corrosion Studies 4
2. Specimen Configuration for Stress Corrosion Test 6
3. Test Equipment 8
4. Three-Point Centrally Loaded Beam 9
5. Stress Relaxation Fringes 12
6. Fringe Pattern, t = 9.1 hrs 12
7. Fringe Pattern, t = 10.8 hrs 13
8. Fringe Pattern, t = 11.8 hrs 13
9. Fringe Pattern, t = 13.8 hrs 14
10. Fringe Pattern, t = 16.8 hrs 14
11. Stress Relaxation With Corrosion Cracking Fringes 15
12. Equipment Arrangement for Aluminum Honeycomb Defect Study 18
13. Location of a Debond in a Honeycomb Panel 20
14. Location of Defect 29 in Elevation 20
15. Defects in a Region of the Trim Tab 21
16. Code for Defect Locations 22
17. Optical Arrangement for Automatic Reference-Beam Compensation 27
18. Experimental Setup For Variable Sensitivity Holographic Interferometry 30
19. Similar Contour Maps Produced With Desensitized Hologram Interferometry 34
20. Result Shown in Figure 19 After Spatial Filtering 34
21. Dissimilar Contour Maps Produced With Desensitized Hologram Interferometry 34
22. Modulated Reference-Wave Holography of Vibrating Loudspeaker 39
23. Expansion of Test Cylinder in the Direction of Sensitivity Vectors $\bar{S}_1$ and $\bar{S}_2$ 42
24. Hologram Apparatus for Pneumatic Testing 42
25. Double Exposure Interferogram 44
26. Flaw Detection Using Vacuum Technique 45
27. Flaw Detection Using Thermal Technique 47
28. Apparatus for Axial Compression Experiments 48
29. Flaw Detection Using Compression Technique 49
30. Vibration Technique 51
31. Experimental Apparatus for Vibration Analysis 53
32. Aerial Images in Hologram Plane 60

TABLES

1. Specimen Exposure Time 16

2. Position and Estimated Size of Suspected Defects (Side 1) 23

3. Position and Estimated Size of Suspected Defects (Side 2) 24

4. Program of Flaws 43

INVESTIGATION OF HOLOGRAPHIC TESTING TECHNIQUES
Semiannual Report
1 June Through 30 November 1969

1
INTRODUCTION

This is the second semiannual technical report on a continuing study of holographic testing techniques which began on 1 December 1968. This report presents technical accomplishments since the last report and discusses preparatory work for further investigation of holographic testing techniques.

Holographic interferometry has been used to detect and monitor, in real time, the initiation and development of stress corrosion cracking in metals. Experiments were conducted with titanium alloys in a methanol atmosphere. The method should be applicable to testing of metals for other delayed cracking phenomena and could possibly lead to greatly reduced testing time.

Holographic interferometry has also been used to detect bond defects in an aircraft trim tab of aluminum honeycomb construction.

Work has continued on the development of pulsed-laser contouring and interferometry. It is hoped that the ability of pulsed lasers to reduce stability requirements will make holography more adaptable to assembly line and in-service testing applications. In this connection, a means of varying the sensitivity of holographic interferometry has been developed.

Preliminary investigations of techniques for improving interferometry of three-dimensional transparent objects are reported.

The extension of modulated reference-wave holography to the study of diffusely reflecting vibrating objects is discussed. This technique may allow the determination of phase information regarding mechanical vibrations and may lead to a new technique of holographic flaw detection.

Further investigation of hologram interferometry for detection of surface flaws in cylindrical steel members, including a critical evaluation of several loading techniques, is included.

2
MONITORING OF STRESS CORROSION CRACKING

A method is being developed for using holographic interferometry to detect initiation and propagation of stress-induced cracks in Ti-6Al-4V alloy submerged in methanol. It is hoped that this technique will be applicable to other stress cracking problems and that it may provide an early indication of flaw development.

2.1. BACKGROUND

2.1.1. DETECTION OF MICROCRACKS

In a previous report [1] we described a holographic method for detecting the presence of fatigue cracks in metal structures. (See also Refs. 2 and 3.) The particular configuration studied involved radial fatigue cracks extending from drilled holes. Holography was used to produce a fringe pattern indicative of the displacement of the surface of the metal member when it was stressed by slightly increasing the torque applied to a tapered-shank bolt inserted in the drilled hole. The presence of a fatigue crack was indicated by anomalies in this fringe pattern. A similar approach was recently reported by Dudderar [4] who visualized the zone of plastic deformation formed near regions of high stress concentration in ductile aluminum alloys subjected to load-unload cycles during which tensile crack opening occurred. Although the objectives and details of these two investigations were different, the optical approach was quite similar.

2.1.2. STRESS CRACKING OF URANIUM ALLOYS

Our investigation of stress cracking detection was stimulated by a materials testing problem described to us by scientific personnel of the Army Materials and Mechanics Research Center. It has been found that certain uranium alloys exhibit a delayed failure due to stress cracking even when stressed far below the tensile yield strength. This phenomenon occurs at normal temperatures in atmospheric air. It has been found that it can be accelerated by increasing the relative humidity. Failure times were indicated by preliminary studies to be on the order of 250 hours.

Delayed cracking phenomena in the uranium-10 w/o molybdenum alloy have been studied and reported by Peterson and Vandervoort [5]. They concluded that the phenomenon was caused by oxygen-embrittlement of the alloy. No delayed cracking occurred in a vacuum, and in their tests moisture was found to delay cracking. They observed that the surfaces of failed statically-loaded tensile specimens were covered with microscopic cracks indicating that crack propagation, rather than initiation effects, is crucial for failure; i.e., that although many cracks are initiated and grow to finite size, embrittlement effects make it possible for only a few to propagate far enough to lead to catastrophic failure.

We intend to develop holographic interferometry as a tool for the study of such phenomena. It is anticipated that holographic techniques may have two major advantages for studying this and related problems.

1. The sensitivity of holographic interferometry might make it possible to detect, or even predict, surface cracking without visual identification.
2. Such tests could be continuously monitored without the necessity of removing the specimen from a high-humidity or otherwise hostile environment as required for visual observation.

2.1.3. STRESS CORROSION CRACKING OF TITANIUM ALLOYS

In order to develop our technique, we decided to study the stress corrosion cracking of another material—preferably a material of some current technical interest which had a fairly short time to failure. This would allow us to conduct a large number of experiments and to develop and refine the technique before attempting to apply it to specimens requiring greater elapsed times to failure. A survey of the literature indicated that titanium alloys in an environment of NaCl, haloginated methanol, or pure methanol exhibited the desired characteristics. For this reason most development of the holographic technique to date has involved observation of titanium alloys in methanol environments.

A brief discussion of stress corrosion cracking of titanium and a brief review of the relevant technical literature is presented in Appendix I.

2.2. HOLOGRAPHIC INTERFEROMETRY

The process of holographic interferometry used in this investigation is essentially equivalent to that described in our previous semiannual technical report [1]. For that reason, a detailed discussion of the basic interferometric technique will not be included here. The major difference in the technique used for stress corrosion cracking observation and that used for microcrack detection is that the former utilizes real-time interferometry while the latter utilizes the double-exposure technique.

The apparatus used in the investigation is shown in Fig. 1. A single hologram of the object in its initial configuration is recorded by simultaneously exposing the film plate to both the object and reference beams. When the plate is developed without altering its position, the optical wavefront stored on the hologram can be reconstructed by illuminating the hologram with the reference beam. If the object is also illuminated, the actual and reconstructed wavefronts will mutually interfere if the object is displaced or distorted in some manner. In this

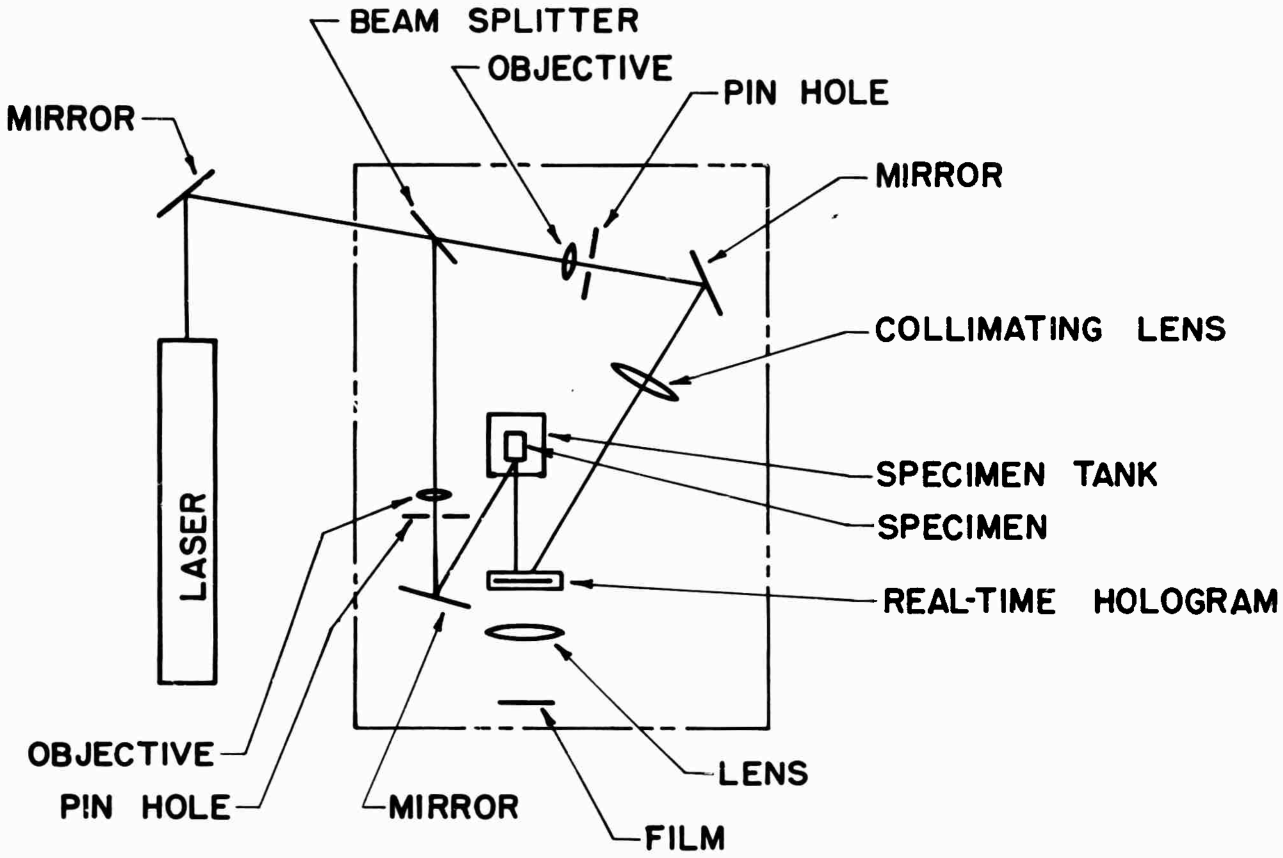

FIGURE 1. OPTICAL ARRANGEMENT FOR STRESS CORROSION STUDIES

investigation the observed interference patterns are indicative of the surface displacement caused by alterations of the stress field associated with the formation and propagation of cracks. Note that these fringe patterns are observed in real time so that the specimen can be continuously monitored.

Further details regarding the optical equipment and holographic technique are presented in Section 2.3.

2.3. EXPERIMENTAL APPARATUS

2.3.1. OPTICAL APPARATUS

The basic experimental setup, which is essentially the same as that described in Ref. [1], is depicted in Fig. 1. Light from the laser is divided by the beamsplitter; one path represents the reference beam and the other the signal beam. Each of the pinhole assemblies consists of a microscope objective and a 15-μm pinhole, and is used to expand the laser beam and to filter extraneous diffraction patterns from it.

During most of this investigation a 20-mW helium-neon laser was used as a light source, and the holograms were recorded on Kodak 649-F spectroscopic plates.

Since holography involves sophisticated interferometric recording, the stringent requirements of interferometry are applicable. Generally, illuminating sources must have sufficient coherence, the entire system must be stable, and the recording medium must have sufficiently high resolution to enable recording of fine interference patterns.

In this application, real-time holographic interferometry is used to continuously monitor crack initiation and propagation. This requires that the photographic plate on which the hologram is recorded be in precisely its original position after it has been developed. If the plate is removed for development it must be realigned to within a fraction of a wavelength of its original position. In order to avoid alignment problems, a plate holder (see Fig. 3b) which allowed the photographic plate to be developed in place was constructed. The glass tank in which the plate is mounted can be filled with developer, fixer, or water. During the exposure and after development, the holder is filled with water. This has two beneficial effects. First, the water causes the photographic emulsion to be sensitized, thereby decreasing the required exposure time by a factor of approximately five. Second, the hologram can be viewed immediately after development, since no drying time is required. Problems of emulsion shrinkage associated with drying are also avoided.

2.3.2. TEST SPECIMEN AND RELATED EQUIPMENT

The test specimen configuration is shown in Fig. 2. The 90° V-notch provides a sufficient stress concentration to cause local plastic strain when the specimen is nominally loaded to the

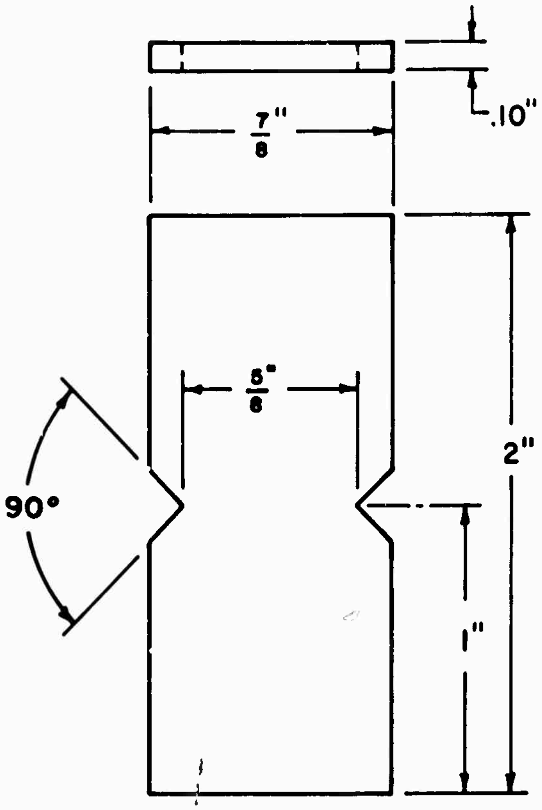

FIGURE 2. SPECIMEN CONFIGURATION FOR STRESS CORROSION TEST. Material is TI-6AL-4V.

yield point. Titanium - 6% aluminum - 4% vanadium in the as-rolled condition is used. This particular alloy was chosen because of its known susceptibility to stress corrosion cracking and its attendant short time-to-failure. In addition, this alloy is of current technical interest because of its use in aircraft and missile components.

The test specimen is stressed in three-point bending by using the simple loading fixture shown in Fig. 3a. During testing this fixture is submerged in a tank filled with methanol. This tank, with the loading fixture in place, is shown at the right of Fig. 3b. The tank has a microflat glass window in order to minimize optical distortion. The tank is carefully sealed to avoid contamination of the methanol by water vapor in the air.

2.4. EXPERIMENTAL PROCEDURE

The titanium specimens were first polished with 500-grit wet sandpaper and cleaned with reagent grade acetone. This was done to remove any protective coating and to make the surface optically diffuse. The specimens were then stressed in the loading fixture as shown in Fig. 4. The maximum nominal tensile stress at the outer fiber was calculated from the equation:

$$\sigma = \frac{6Eh\delta}{L^2}$$

where σ = stress (psi)
E = modulus of elasticity

When the stress in the specimen exceeded the yield stress the part was observed to relax with time. Obviously this relaxation is indicated by interferometric fringes if it occurs during testing of a specimen. Since it is undesirable to have this process occurring while the specimen is being examined for stress corrosion cracking, the specimen was first stressed but not submerged in methanol. A hologram was recorded, and the relaxation was observed by real-time holographic interferometry. When the resultant fringe pattern became stationary, relaxation was concluded and the stress corrosion tests were started.

The loaded specimen was placed into the tank which was then filled with anhydrous, reagent grade methanol. The tank was then carefully sealed to avoid significant water-vapor contamination of the methanol, because such contamination is known to suppress the stress corrosion process. Once the specimen was submerged, a hologram of the specimen was recorded. The plate was then developed in place, as described in Section 2.3.1.

When the illuminated specimen and reconstructed hologram were simultaneously viewed, a fringe pattern, which changed with time, was observed to be superimposed on the specimen. This pattern was indicative of the stress corrosion cracking process. The fringes were

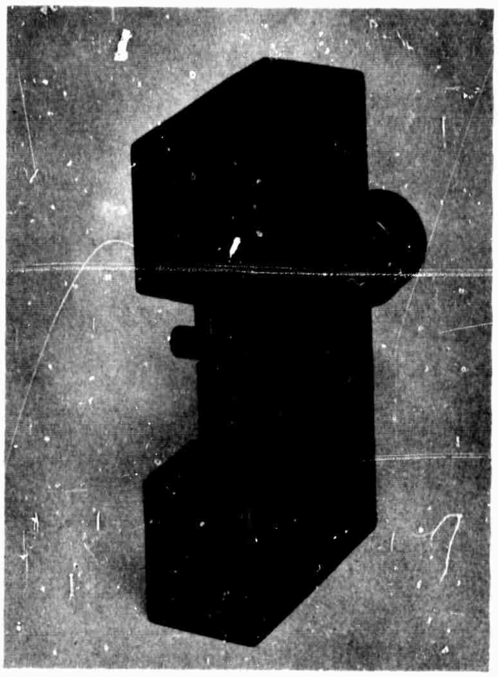

(a) Test Specimen and Loading Fixture

(b) Real-Time Plate Holder and Specimen Tank

FIGURE 3. TEST EQUIPMENT

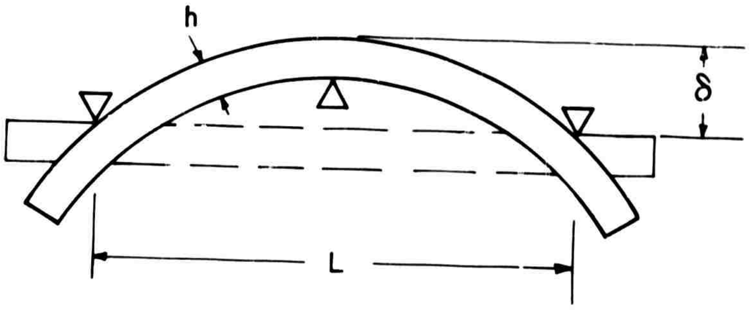

FIGURE 4. THREE-POINT CENTRALLY LOADED BEAM

photographed at various times during the test. The results of a typical test are presented in the next section.

2.5. EXPERIMENTAL RESULTS

In this section typical results of an observation of stress corrosion cracking are presented. Figures 6 through 10 are photographs of fringe patterns at various times during the test. Information regarding these observations is presented in Table 1.

As indicated above, the specimen was first nominally stressed to approximately the yield point. Holographic interferometry was then used to check for stress relaxation before subjecting the specimen to methanol. Figure 5 shows a typical interference pattern indicating the surface displacement as the specimen relaxes. These fringes indicate that the entire surface is affected in a fairly uniform manner. This pattern should be contrasted with those discussed below. After this fringe pattern ceased to change with time, the stress corrosion cracking test was started.

Figures 6 through 10 show the fringe patterns observed at various stages of crack initiation and propagation in a specimen. In this particular experiment very little activity was observed until several hours after the specimen was submerged in methanol. The hologram used to produce these fringes was recorded nine hours after the specimen was first exposed to the methanol. Figure 6 shows an early indication of stress corrosion activity. Note that the deformation is obviously initiated at the notch on the left side. This is presumably an early indication that stress corrosion is occurring in that region of stress concentration. In other tests this initiation occurred near the other notch or simultaneously near both notches.

Figures 6-10 show the progressive change in the fringe pattern during the stress corrosion cracking process. The times at which these patterns were recorded are indicated in Table 1. Only in the last two figures were cracks clearly visible to the unaided eye; the fringes in these last figures were too fine to be readily photographed with a simple camera.

In the experiment described above we were careful to separate the effects of stress relaxation and stress corrosion cracking. Though desirable, this separation is not necessary if relaxation is not so great as to produce extremely fine fringes. Figure 11 is a typical fringe pattern produced when the loaded specimen is submerged in methanol before stress relaxation occurs. This pattern is clearly an indication of simultaneous stress relaxation and stress corrosion crack initiation. Note that corrosion cracking appears to be initiated near both notches. This specimen did, in fact, eventually crack on both sides.

No effort was made to precisely evaluate the surface displacements indicated by the fringe patterns. They are considered as qualitative visualizations of the progress of stress corrosion cracking. Basically, however, the fringes are lines of constant surface displacement relative to the surface configuration when the hologram was recorded. For the particular experiment described above each fringe represents a displacement of roughly 0.3 μm.

2.6. CONCLUSIONS

The results reported in the previous section indicate that holographic interferometry can be used to monitor delayed cracking phenomena such as stress corrosion cracking. The variation of interferometric fringes with time in a sense indicates a "degree" of stress corrosion attack as a function of time. The probable region of crack initiation can be located before an observable macroscopic crack appears. The method may therefore prove to be useful in studying the susceptibility of materials to delayed cracking without having to wait for actual failure.

There are, however, certain limitations which should be noted. First, the mechanical stability requirements inherent in real-time interferometry discussed earlier must be satisfied. Second, the environment of the specimen must be transparent to laser light so that the object may be observed, and it must remain at constant temperature to avoid extraneous fringes. Finally, no gross corrosion of the surface can occur. If it does, the optical correlation between the hologram and the surface will be lost and meaningful interferometric fringes will not be produced.

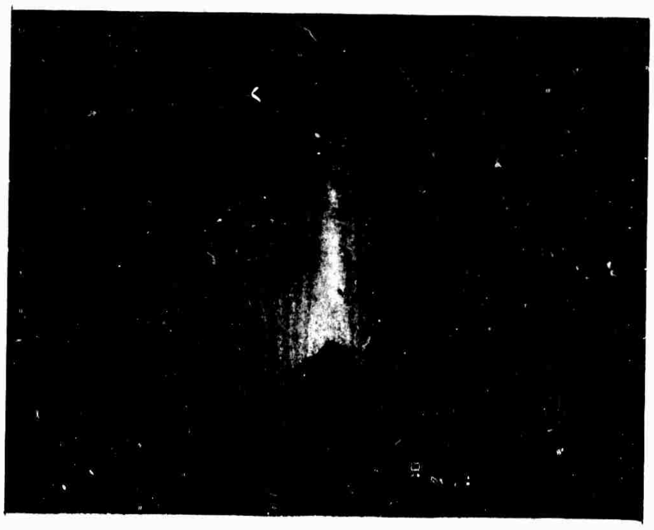

FIGURE 5. STRESS RELAXATION FRINGES

FIGURE 6. FRINGE PATTERN, t = 9.1 hrs

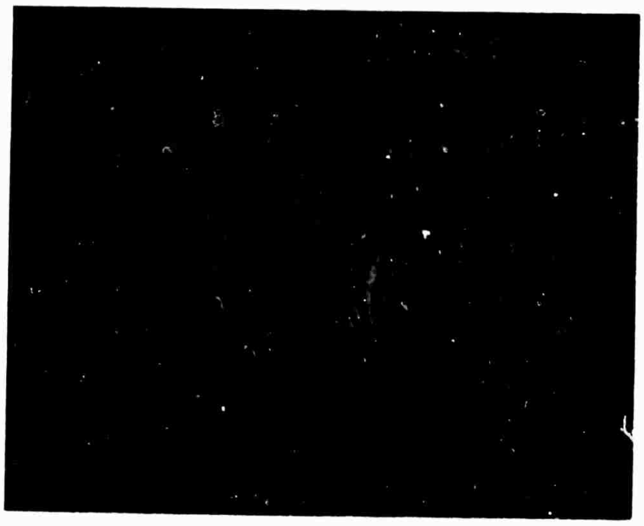

FIGURE 8. FRINGE PATTERN, t = 11.8 hrs

FIGURE 7. FRINGE PATTERN, t = 10.8 hrs

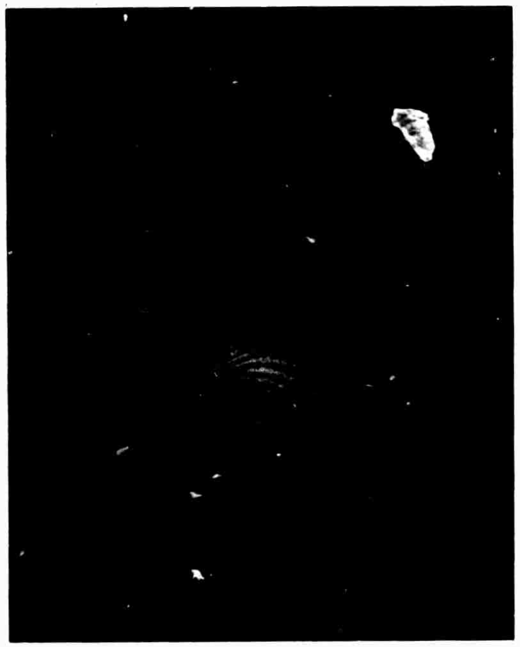

FIGURE 9. FRINGE PATTERN, t = 13.8 hrs

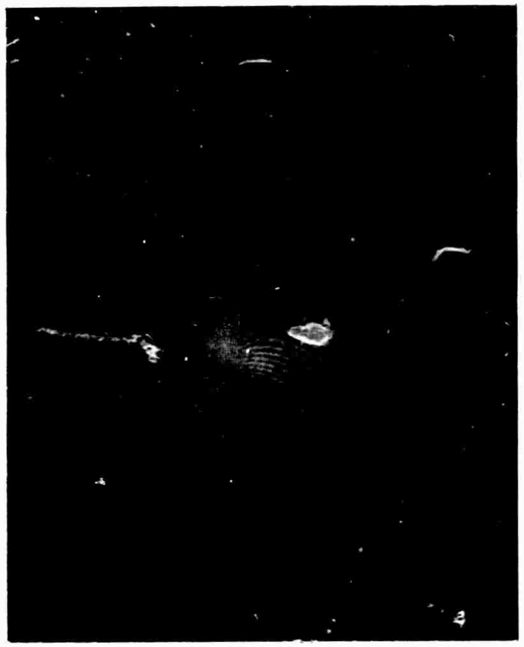

FIGURE 10. FRINGE PATTERN, t 16 8 hrs

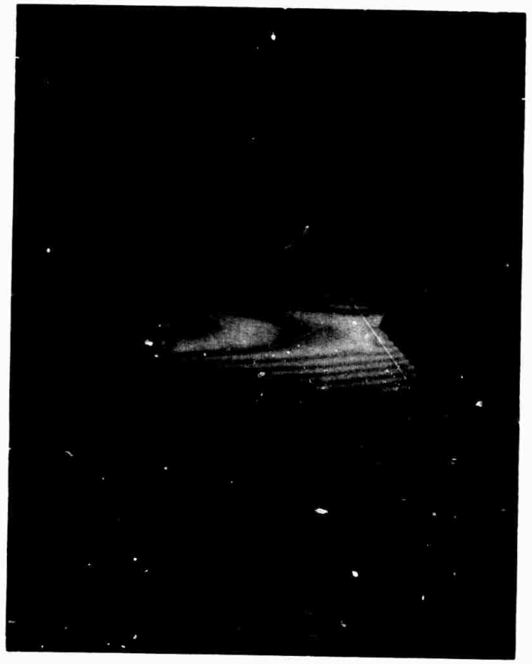

FIGURE 11. STRESS RELAXATION WITH CORROSION CRACKING FRINGES

TABLE 1. SPECIMEN EXPOSURE TIME

Figure	Time at which fringes were photographed (hr)	Time at which hologram was recorded (hr)	Remarks
6	9.1	9	No crack visible
7	10.8	9	No crack visible
8	11.8	9	No crack visible
9	13.8	9	1/16-in. crack visible
10	16.8	9	1/8-in. crack visible

3

HOLOGRAPHIC TESTING OF HONEYCOMB SANDWICH AIRCRAFT STUDIES

3.1. INTRODUCTION

An investigation of the use of holographic interferometry to locate defects in an aircraft trim tab of honeycomb construction was carried out with the co-operation of Lt. James W. Bohlen of the Air Force Materials Laboratory (MAMN), Wright-Patterson Air Force Base, who made the aircraft component available to us. Although a similar method for testing honeycomb material has been reported elsewhere [6], this brief investigation was of importance since it offered an opportunity to apply holography to an actual structure in which debonds are of concern. The aircraft component was subjected to a large variety of testing techniques and will eventually be destructed in such a manner that flaws will be located and measured. A quantitative comparison of the results of our holographic investigation with other techniques will be reported later.

3.2. EXPERIMENTAL APPARATUS AND PROCEDURE

The basic layout of the experimental equipment is depicted in Fig. 12. Optically, this is a system for carrying out real-time holographic interferometry similar to that discussed in Section 1 of this report. The object is an aircraft trim tab constructed by bonding a relatively thin metal skin onto an aluminum honeycomb core. The surface of the part was not painted or prepared in any special manner for these tests.

In order to detect faulty bonds between the honeycomb core and the skin, a hologram of the test region was recorded in the usual manner. With this simple setup we were able to record a hologram of one third of the 3-ft-long surface of the component. The plate was then developed without being moved from its original position. When the developed holographic plate is illuminated by the reference beam (ABC), the first diffracted order emanating from the hologram exactly reproduces the original wave pattern of the light scattered by test areas of the aircraft elevator. If the surface of the elevator is then distorted in some manner, the resulting new wavefront will combine with the holographically reconstructed wavefront to form an interference pattern. The fringe location and density of this pattern can then be related to the displacements of the test region. This technique is known as real-time holographic interferometry.

In this experiment the holographic plate was developed and the elevator was then irradiated from behind with a 150-W infrared lamp. The heat from the lamp was conducted to the front

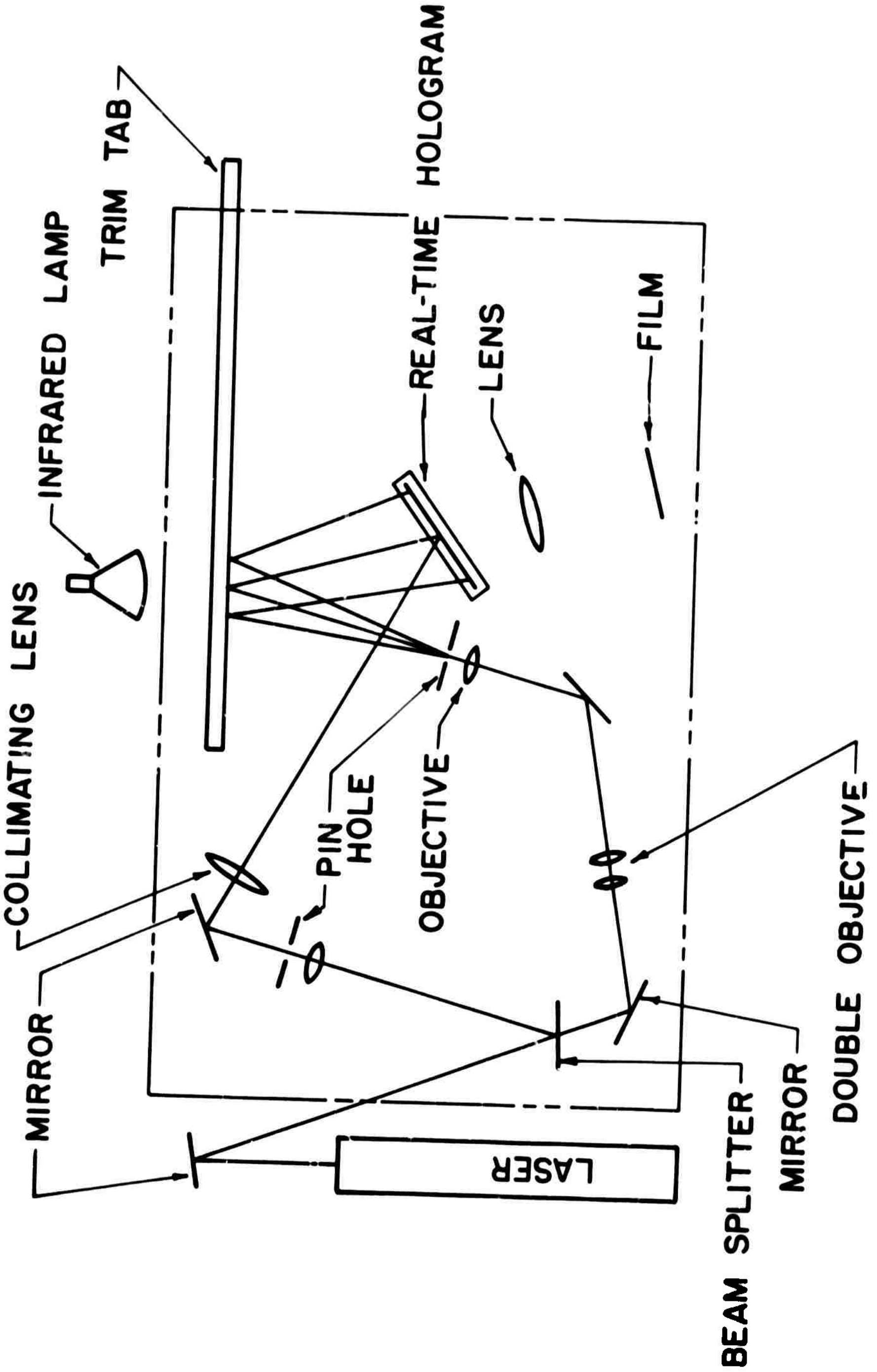

FIGURE 12. EQUIPMENT ARRANGEMENT FOR ALUMINUM HONEYCOMB DEFECT STUDY

skin of the elevator in less than one second. Since the thermal strain* in the skin is related to the temperature variations in the structure, subsurface defects can be detected if they sufficiently affect the temperature distribution on or near the surface.

3.3. EXPERIMENTAL RESULTS

The fringe anomalies resulting from the presence of defects were found to be most apparent when the skin of the trim tab was conducting heat transiently in the lateral directions. During this time, the fringe pattern consisted of a growing set of approximately circular fringes spreading radially from the center of the heated region. As a given fringe reached the vicinity of a defect it became locally wavy, sometimes forming a closed loop around the defective area. Figure 13 shows such an anomalous pattern near a large defect in a honeycomb panel used to check the procedure prior to testing the elevator itself. Apparently, the outermost rings show the approximate outline of a debond.

Figures 14, 15a, and 15b show defects in the aircraft trim tab — Fig. 14 shows defects 29 and 30; Fig. 15a shows defects 18, 19, 20, 21, 23, 25 and 31; and Fig. 15b outlines the defects in 15a. The defect numbers refer to Fig. 16 and Tables 2 and 3. The fringe anomalies in the photographs are not nearly as pronounced as they appeared when viewed directly by the eye.

Tables 2 and 3 indicate the position and size of the suspected defect locations as determined by holographic interferometry.

---

*Note that the fringe pattern is a mapping of the surface displacement field rather than the strain field.

FIGURE 13. LOCATION OF A DEBOND IN A HONEYCOMB PANEL

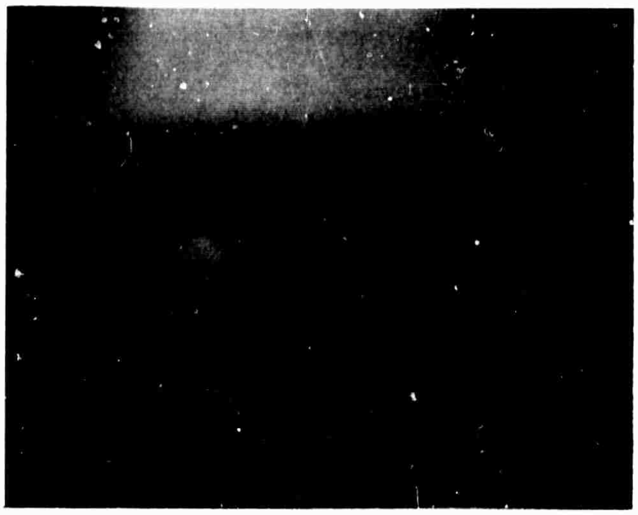

FIGURE 14. LOCATION OF DEFECT 29 IN ELEVATION

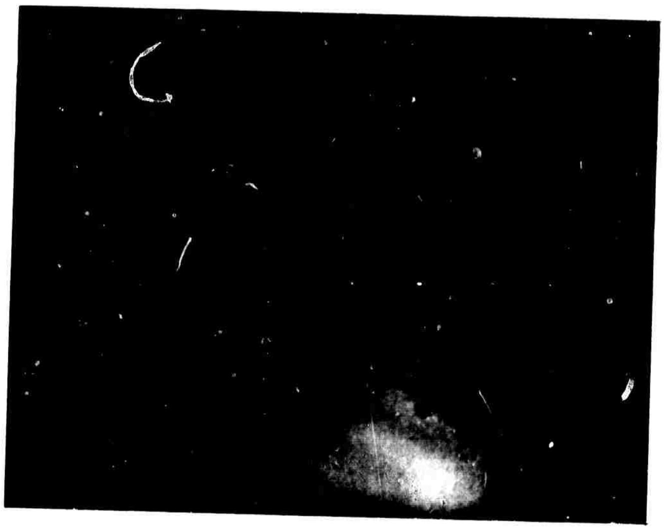

(a) Location of Defects

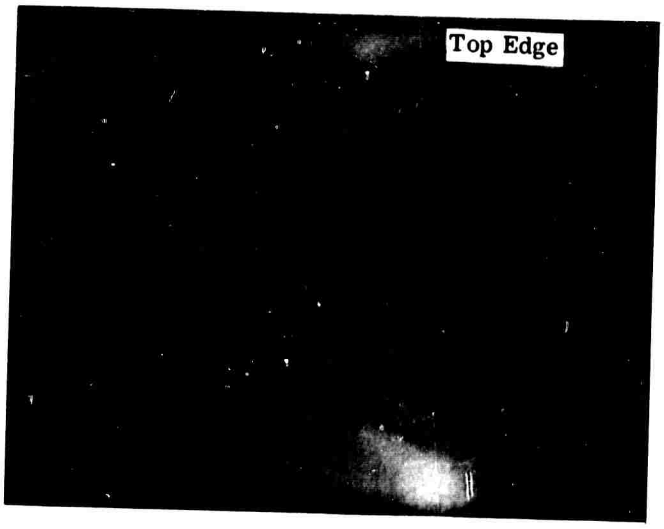

(b) Outline of Defects

FIGURE 15. DEFECTS IN A REGION OF THE TRIM TAB

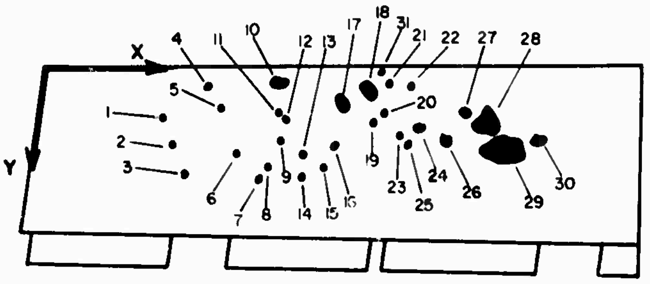

(a) Side 1

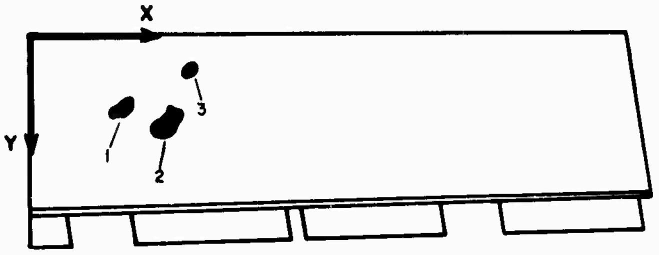

(b) Side 2

FIGURE 16. CODE FOR DEFECT LOCATIONS

TABLE 2. POSITION AND ESTIMATED SIZE OF SUSPECTED DEFECTS (Side 1)

Defect	x coordinate to center of defect	y coordinate to center of defect	Approximate diameter to nearest 0.25 in.	Remarks
1	8.5	3.25	0.25	*
2	9.5	4.75	0.25	*
3	10.5	7.0	0.5	*
4	11.5	1.0	0.5	
5	2.25	2.5	0.25	
6	13.5	5.5	0.5	
7	15.25	7.0	0.25	*
8	15.5	6.25	0.25	*
9	16.25	4.5	0.25	*
10	16.0	1.0	1.0	
11	16.25	3.0	0.25	*
12	16.50	3.25	0.25	*
13	17.75	5.5	0.50	
14	17.75	6.75	0.50	
15	19.0	6.5	0.25	*
16	19.5	5.25	0.25	*
17	20.0	2.25	1.0	Elliptical
18	21.5	1.25	1.0	Elliptical
19	22.0	3.5	0.25	*
20	22.75	2.75	0.25	*
21	23.0	1.0	0.25	
22	24.5	1.0	0.50	
23	23.75	4.25	0.50	
24	25.0	3.75	0.75	
25	24.0	4.5	0.25	*
26	26.5	4.5	0.75	
27	27.75	2.75	0.75	
28	29.0	3.5	1.5	Kidney shaped
29	30.0	5.0	2.0	Elliptical shape Max: 2.75 Min: 1.50 (Largest Defect)
30	32.25	4.5	0.50	
31	22.5	0.25	0.75	

---

*These defects were not as pronounced during the tests as the others. Without past experience, it is impossible to determine whether these are debond defects, defects in the honeycomb structure, defects in the skin material, or false indications.

TABLE 3. POSITION AND ESTIMATED SIZE OF SUSPECTED DEFECTS (Side 2)

Defect	x coordinate to center of defect	y coordinate to center of defect	Approximate diameter	Remarks
1	5.5	5.0	0.25	*
2	7.75	5.0	0.25	*
3	8.0	2.0	1.0	†

---

*These defects were not as pronounced during the tests as the others. Without past experience, it is impossible to determine whether these are debond defects, defects in the honeycomb structure, defects in the skin material, or false indications.

†This defect is opposite the largest defect on side 1 (i.e., defect 29); this indication may be an image of 29 and not a defect.

4
PULSED-LASER HOLOGRAPHY

4.1. INTRODUCTION

The work described in this section and in Section 5 deals with the general area of multiple-wavelength holographic interferometry (MWHI). Although many of the results reported here are of general utility in the field of holographic interferometry, this work has been undertaken primarily to develop methods of producing pulsed-laser contour maps and interferograms. The ultimate development of these methods should enable one to greatly reduce mechanical stability requirements of interferometry and make contouring and interferometry readily available for assembly line and in-service testing and measurement applications.

Just as in ordinary holographic interferometry [7], either transparent or opaque objects can be examined. So far, however, our most important results have dealt with producing contour maps of opaque objects. Our primary efforts have been directed toward (1) improving the technique of obtaining MWH interferograms, and (2) investigating a specific application of the MWH interferometry.

4.2. MULTIPLE-WAVELENGTH HOLOGRAPHIC INTERFEROMETRY

4.2.1. PULSED-LASER HOLOGRAPHIC CONTOURING

We have not yet obtained a pulsed laser capable of producing two different frequencies simultaneously. We plan to modify our ruby laser by the intracavity insertion of a quarter-wave plate. Properly adjusted, this plate should allow us to obtain the ruby R_1 and R_2 lines ($\Delta\lambda \cong 14\text{Å}$). Such a wavelength difference would give a contouring interval of about one-tenth of a millimeter. This modification has been delayed because of difficulty in obtaining the specially-cut wave plate. In the meantime, we have been investigating the concepts discussed below which will be very useful (if not necessary) for doing pulsed-laser contouring with widely separated wavelengths.

4.2.2. AUTOMATIC REFERENCE-BEAM COMPENSATION

The technique of multiple-frequency contouring by image plane holography [8, 9] has been an important improvement in holographic contouring. One main disadvantage of the technique is that it still requires a precise manual realignment of the reference beam between the two exposures.

As part of our program to develop a practical technique for obtaining multiple-frequency holographic contour maps, an optical setup is being tried which should automatically give the correct change in offset angle for any change in laser frequency. Preliminary results have been positive, but considerable additional work is needed. This automatic correction will be necessary for the planned pulsed-laser contouring work.

Figure 17 gives a simple diagram of the new method. The optical setup is conceptually identical to that setup described in previous reports on multiple-frequency contouring by image plane holography [9].

Reference 9 describes a technique for obtaining depth contours by multiple-frequency holographic interferometry. The important features of the technique are:

(1) Plane wave reference beams: Only by using plane wave reference beams will a simple change in offset angle cause interference to occur over the whole object.

(2) Telecentric imaging of the object onto the hologram: This action minimizes the aberrations and distortions of reconstructing a hologram with a wavelength different from that used in constructing the hologram. It also minimizes the accuracy needed in making the above change in offset angle. The telecentric viewing simply means that the object is viewed and imaged as it is illuminated—parallel to the axis of the telescope. Telecentric viewing is also important in making only one change in offset angle for all object points.

The important change is the use of a grating to bend the plane wave reference beam onto the hologram. Our objective is to have the average spatial frequency of the interference fringes be independent of the laser frequency used.

This objective is obtained very simply. The system is arranged so that the telescopic axis and the plane wave reference beam are parallel. The grating and the hologram are also made parallel to each other and normal to the telescopic axis. When the grating bends the reference beam by a given angle, one can see that the diffracting geometry and recording geometry are identical. Thus, independent of the laser frequency, the holographic carrier frequency will match the frequency of the grating. A detailed discussion of the theory of this technique is presented in Appendix II.

4.2.3. NONLINEAR RECORDING

We plan to adapt some recently reported [10] applications of nonlinear hologram recording to multiple-wavelength holographic interferometry. The goal is to generate higher order multiples of the phase variations caused by the object (whether opaque or transparent). This will allow us to (1) obtain interferograms of increased sensitivity, and/or (2) obtain fringe sharpening if techniques can be found for superposing the interferograms of all n-orders.

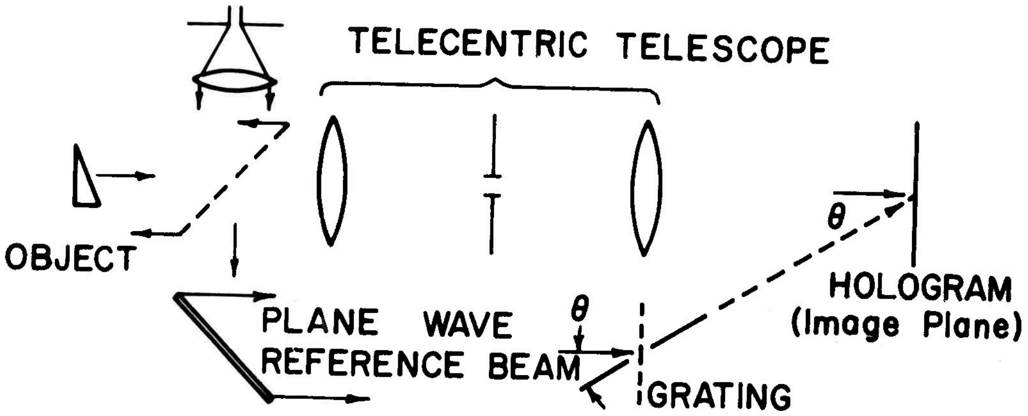

FIGURE 17. OPTICAL ARRANGEMENT FOR AUTOMATIC REFERENCE-BEAM COMPENSATION

The optical setup should be an easy adaptation of the setup described in Section 5. The chief modification will be to make the offset angle very small so that higher order images will be more easily obtained. The nonlinearities will be brought out by bleaching the holograms.

When one bleaches a hologram, the effect is to convert the light-absorbing silver particles in the emulsion into transparent particles with a refractive index different from that of the emulsion. In a typical hologram, the complex amplitude transmittance is a real-valued function of the form

$$T_A = |u_o|^2 + |u_r|^2 + 2|u_o||u_r| \cos \phi$$

where u_o and u_r are the respective complex amplitudes of the signal and reference beams and where ϕ is the relative phase between the signal beam and the reference beam.

After bleaching, the hologram transmittance becomes (ideally) a pure phase function

$$T'_A = \exp (ibT_a) = K \exp (ib2u_o u_r \cos \phi)$$

where K and b are factors which need not be discussed here. Note now that we can expand this last expression in the following form:

$$T'_A = K \sum_{n=-\infty}^{\infty} J_n(b2u_o u_r) \cos n\phi$$

where J_n is a Bessel function of the first kind. Obviously, we now have an infinite number of terms containing $|u_o|$ and ϕ which relate to the amplitude and phase of the object wavefront in the hologram plane. In order to be instructive, we will omit consideration of certain details and consider only the phase term:

$$\cos n\phi = \frac{\exp (jn\phi) + \exp (-jn\phi)}{2}$$

where $\phi = \alpha x - \theta(x)$, α being a spatial carrier and $\theta(x)$ being the object phase (in the near image-plane case). Upon reconstruction, we obtain an image term of the form

$$\exp [jn\theta(x)]$$

so that if $\theta(x)$ represents some change in phase caused by the object, the recording process has given us a term n-times more sensitive to such changes. We feel this would give a considerable improvement in the usefulness of multiple-wavelength holography interferometry.

5

VARIABLE SENSITIVITY HOLOGRAPHIC INTERFEROMETRY

5.1. INTRODUCTION

Hologram interferometry [7] has been shown to be a useful technique for determining the displacement fields of diffusely reflecting objects. The method is extremely sensitive; it is capable of measuring displacements on the order of 0.3 μm. It is obvious that for the many applications which require the measurement of displacements on the order of millimeters or centimeters, standard hologram interferometry is too sensitive to be useful, since the fringes become too fine to resolve. We have, therefore, started an experimental and theoretical study of the use of multiple-wavelength holography [8, 9, 11, 12] to perform desensitized hologram interferometry. Desensitized hologram interferometry should be useful for studying objects subjected to large deformations by static loads, steady-state vibrations, or transient events of many types. A short analysis of one of the simplest possible static loading cases has been completed, and experiments have been performed to support the conclusions of this analysis.

Both the analysis and the experiments are concerned with cases where all object-point displacements are assumed to be in one direction. In ordinary hologram interferometry the distance between two fringes corresponds to a displacement sensitivity on the order of $\lambda/2$. By using multiple-wavelength holography, we have demonstrated a displacement sensitivity on the order of $\lambda_1\lambda_2/2(\lambda_2 - \lambda_1)$; the quantity $\lambda_1\lambda_2/2(\lambda_2 - \lambda_1)$ is never smaller than $\lambda_1/2$ where λ_1 is less than λ_2.

5.2. THEORY

An optical setup similar to that shown in Fig. 18 will be analyzed and used in our experimental work. Previously [5], a detailed description has been given of the operation of this setup for making contour maps by the multiple-refractive-index technique; therefore, we will give only a brief description here.

A contour map of the surface of an object can be produced by reconstructing a double-exposure hologram of the object. For each exposure the immersion tank is filled with a fluid with a different index of refraction. A carefully-aligned collimated beam illuminates the tank normal to its transparent side. The viewing system is arranged so that each object point can be seen only by light rays reflected almost parallel to the illumination beam. It is convenient to select a coordinate system with its origin at the intersection of the optical axis and the inner surface of the immersion tank. The x-y plane is taken to lie in the plane of the inner surface; the z-axis is therefore parallel to both the illumination beam and the line of sight. Thus, the effective change between the two exposures is in the axial optical path length traversed from the inner surface of the tank to the object and back.

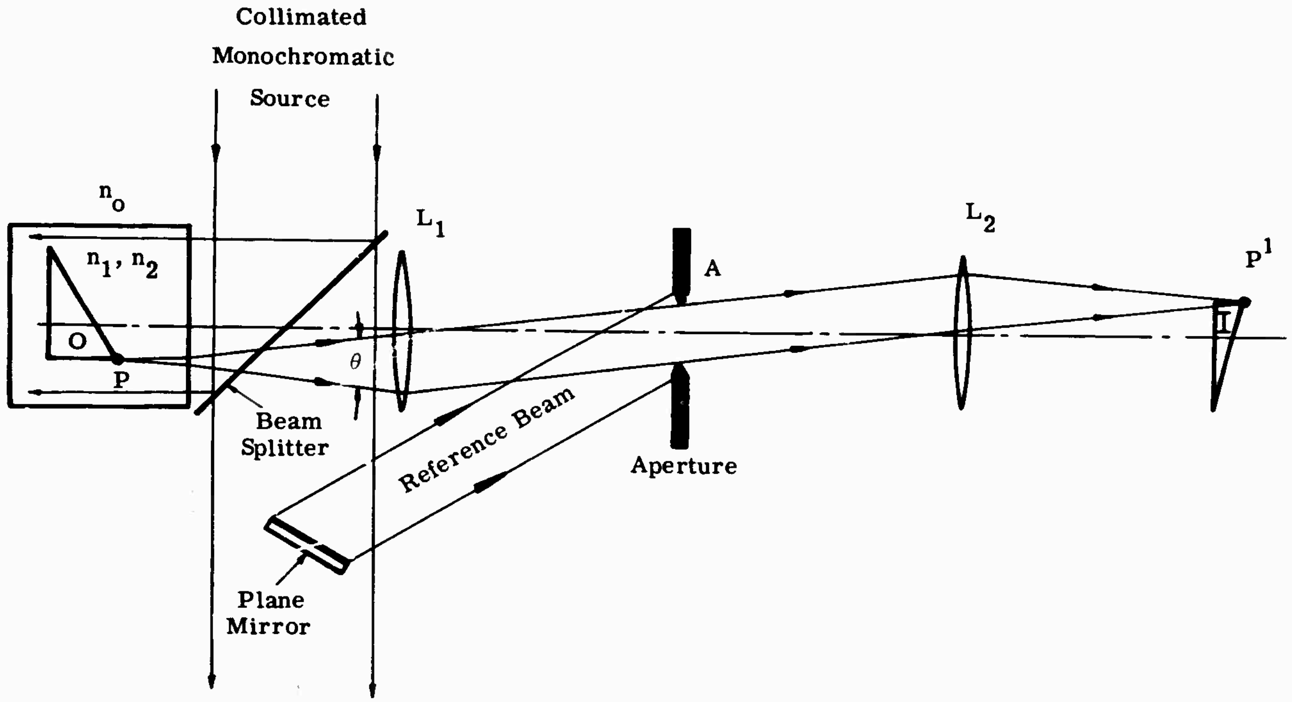

FIGURE 18. EXPERIMENTAL SETUP FOR VARIABLE SENSITIVITY HOLOGRAPHIC INTERFEROMETRY

Upon reconstruction of the hologram, we have two wavefronts interferring in the image plane of the viewing system:

$$U_I = S_{1(x,y)} \exp[j2k_1 z(x, y)] + S_2(x, y) \exp[j2k_2 z(x, y)] \tag{1}$$

where U_I = the sum of the complex amplitudes of the two reconstructed wavefronts at the image plane, $S_1(x, y)$ and $S_2(x, y)$ are directly related to the object brightness at (x, y) for the two different exposures, k_1 and k_2 are the respective wave factors of the two different fluids, and z(x, y) is the axial coordinate of the object point at (x, y).

In practice, $S_1(x, y)$ and $S_2(x, y)$ are almost identical. By using a uniform illumination beam and by treating the object surface (in any permissible manner) to make it diffusely reflecting, we can usually make S_1 and S_2 very slowly varying functions. This procedure places the contour fringes on a much less confusing background. With these thoughts in mind, we arrive at the intensity of the image:

$$|U_I|^2 = 2S_1^2[1 + \cos 2(k_2 - k_1)z(x, y)] \tag{2}$$

Thus, for any set of lateral object coordinates (x^*, y^*), the reconstructed image brightness is modulated according to the axial coordinate, as shown by the above expression for $|U_I|^2$. The overall result is a depth contour map of the object.

The simple analysis we have performed is concerned with measuring a displacement along the axis (i.e., Δz). This can be done by making two depth contour maps of the object; the displacement of any point can then be found by fringe counting. But, since fringe counting could be very tedious, we would prefer to find some convenient means of getting a direct display of the displacement information. A means of obtaining such a display which is often satisfactory is to overlay the two contour map transparencies to produce a moiré fringe pattern. Adding the two contour maps, we obtain

$$\begin{aligned} |U_{I1}|^2 + |U_{I2}|^2 &= S_1^2[4 + 2\cos 2\Delta k z_1(x, y) + 2\cos 2\Delta k z_2(x, y)] \\ |U_{I1}|^2 + |U_{I2}|^2 &= 4S_1^2[1 + 1 \cos \Delta k \Delta z \cos \Delta k \Sigma z] \end{aligned} \tag{3}$$

where $\Delta k = k_2 - k_1$

$\Sigma z = z_2 + z_1$

$\Delta z = z_2 - z_1$.

In some cases, one might find considerable advantage in making a four-exposure hologram. This four-exposure procedure eliminates any errors in the moiré fringe pattern which might be caused by misalignment of the two contour maps. From the four-exposure hologram we reconstruct:

$$U_{I1} + U_{I2} = S_1 \left[\exp\left(i2k_1z_1\right) + \exp\left(i2k_2z_1\right) + \exp\left(i2k_1z_2\right) + \exp\left(i2k_2z_2\right)\right]$$

The intensity of the image in this case is of the form:

$$\left|U_{I1} + u_{I2}\right|^2 = 4S_1^2\left[1 + \frac{1}{2}\cos \Sigma z\Delta k \left(\cos \Sigma z\Delta k + \cos \Sigma k\Delta z\right) + \frac{1}{2}\cos \Sigma z\Delta k \cos \Sigma k\Delta z\right] \qquad (4)$$

The factor of interest is (in both cases)

$\cos \Delta k\Delta z$

which has a period of $\lambda^2/\Delta\lambda$. This factor gives the desensitized interferometry information. The term $\cos \Sigma z\Delta k$ corresponds to an average contour modulation and $\cos \Delta z\Sigma k$ corresponds to an average hologram interferometry modulation.

Equation (4) assumes that the interference between the four terms in independent of the fine surface structure of the object. Further analysis is needed to determine if this is true; it is not known whether or not the reflected wavefront from the object resolution cell seen at (x^*, y^*) in one load condition and the reflected wavefront seen at (x^*, y^*) in the second condition are correlated within the depth of field of the optical viewing system. If they are not, no meaningful interference could take place to indicate the object displacement by the usual hologram interferometry. We would then obtain the same expression obtained for overlaying two contour map transparencies:

$$\left|U_{I1} + U_{I2}\right|^2 = 4S_1^2\left[1 + \cos \Delta z\Sigma k \cos \Sigma z\Delta k\right]$$

Before the surface correlation question and others can be answered, object shapes, surface structures, and displacements will have to be categorized. Then definite statements can be made about the advantages of desensitized hologram interferometry.

5.3. EXPERIMENTAL RESULTS

We picked a simple object—a cantilever beam—for our first experiments with desensitized hologram interferometry. The multiple-index contouring technique was used because of its simplicity and its available range of contouring intervals.

Figure 19 shows a clear set of desensitized fringes on the cantilever beam (the beam is about 1/16-in, thick, 3/4-in. wide, and 4-in. long). Load condition 1 had a total end-to-end displacement of about 1/4 in., and we count about 100 contour fringes end-to-end. By counting moiré fringes, we see that condition 2 had 16 more (or fewer, since an ambiguity exists without previous knowledge) fringes. The end displacement was actually about 3/40 in. Thus, the experimental value for the equivalent wavelength is:

$$\frac{\lambda_{eq}}{2} \sim \frac{3/40}{16} \cong \frac{3}{640} \cong \frac{1}{210} \cong 0.005 \text{ in.}$$

whereas $\frac{\lambda}{2} = \frac{0.63\ \mu m}{2} = 0.31\ \mu m \cong 0.000015$ in., which indicates a desensitization factor of 300.

The two liquids used in obtaining the result shown in Fig. 19 were water and a 12% solution of ethyl alcohol in water. The refractive index of water is about 1.33 and that of ethyl alcohol is about 1.36. The difference is 0.03 and about one-tenth of that difference was assumed to exist between water and the 12% solution. Thus,

$$\frac{\lambda}{\Delta n} = \frac{\lambda}{0.003} = 333\ \lambda$$

where λ is the light wavelength in air.

As previously stated, the contouring interval is

$$\frac{\lambda^2}{n_1 n_2} \Bigg/ \frac{\lambda}{n_1} - \frac{\lambda}{n_2} = \frac{\lambda}{\Delta n}$$

We find that our tacit assumption of a linear variation of refractive index with percent concentration was good for small percentages. Of course, in practice, we would want more accurate refractive indices.

The moiré fringe contrast can be increased by recording the contour maps on higher contrast film and, sometimes, by using optical spatial filtering. The result shown in Fig. 19 was obtained by making four exposures on one hologram with the same reference wavefront. Figure 20 shows the moiré fringes in much higher contrast after spatial filtering; the large speckle effect is due to the lowpass filter used in this case. We could observe no indication of the extra terms predicted in Eq. (4). This would imply that either the extra terms were of too high a spatial frequency to be resolved or that due to an addition of the uncorrelated surface structure image the extra terms did not exist in the region of focus. We tried to repeat this experiment with ordinary hologram interferometry; we could observe fringes only in the area of minimum displacement very near the clamped portion of the cantilever beam. The expected average spatial frequency of the fringes was about 50 lines/mm and our optical system had a resolution capability on the order of 200 lines/mm; therefore, we think the lateral surface structure displacement may have been the important factor in this case. More work in this interesting area will be necessary before conclusive statements can be made

The result shown in Fig. 19 was for the case where the two contour maps were very similar. Figure 21, on the other hand, shows a result where the two contour maps were very different. The moiré fringes are quite hard to see in this photograph, but they are visible in the region of minimum displacement. An extreme example of very different contour maps is

FIGURE 19. SIMILAR CONTOUR MAPS PRODUCED WITH DESENSITIZED HOLOGRAM INTERFEROMETRY

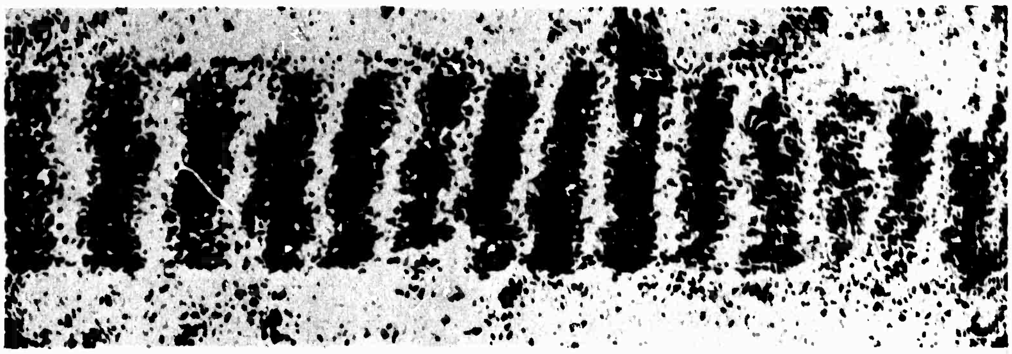

FIGURE 20. RESULT SHOWN IN FIGURE 19 AFTER SPATIAL FILTERING

FIGURE 21. DISSIMILAR CONTOUR MAPS PRODUCED WITH DESENSITIZED HOLOGRAM INTERFEROMETRY

obtained when a flat object normal to the z-axis is loaded and unloaded; the contour map of the loaded object then is the desensitized fringe system.

5.4. CONCLUSIONS

Our work is at such an early stage that we can conclude only that desensitized hologram interferometry holds great promise for extending the range of applications of hologram interferometry.

6

INTERFEROMETRY OF THREE-DIMENSIONAL TRANSPARENT OBJECTS

6.1. INTRODUCTION

In our previous report [1] we discussed the application of holographic interferometry to the study of transparent objects subjected to mechanical loading. A brief discussion and analysis of fringe localization in such objects was also presented. We found that in order to obtain partial information about index of refraction changes in a third dimension (as opposed to strictly two-dimensional information accessible to classical interferometry) it is necessary to utilize diffuse illumination. In practice, this generally means that a laser-illuminated frosted glass is used to provide background illumination. This diffuseness introduces the problem of laser speckle into interferometry of transparent objects. Speckle is a grainy pattern inherent in any image of a coherently-illuminated diffuse object. Physically, this speckle is simply the random interference pattern formed by the light scattered from various points on the object. It has been discussed by Goldfischer [13], and its effect on fringe visibility in holographic interferometry has been considered by Tanner [14].

We have given preliminary consideration to eliminating some of the undesirable effects of laser speckle in interferometry by developing schemes to do the following:

(1) Introduce a different type of background illumination which might eliminate laser speckle, improve fringe resolution and visibility, and enable one to still view the object from arbitrary directions.

(2) Eliminate laser speckle but allow only a finite number of viewing directions.

Concepts which may make these improvements possible are discussed below.

6.2. POSSIBLE IMPROVEMENT OF FRINGE VISIBILITY AND RESOLUTION

Leith and Upatnieks [15] have recently discussed a means of improving imagery with coherent illumination by using pseudo-randomly diffused illumination. This involves an illumination which is intermediate to the limiting cases of plane wave illumination and randomly diffused illumination such as that obtained with an etched glass diffuser. Their illumination is derived from a diffuser of known structure—the simplest example is a crossed diffraction grating. Theoretical criteria are presented for the form of illumination which allows formation of a noise-free image of a given plane in a semi-transparent object. That is in theory both the diffraction noise associated with plane wave (or uniform wavefront) illumination and the speckle associated with randomly diffused illumination can be eliminated while imaging a particular plane.

We have initiated some simple preliminary experiments to determine if background illumination of this nature might improve interferometry of three-dimensional objects. Using a simple crossed grating to "diffuse" the light passing through the object effectively replaces the random speckle pattern with a very fine, orderly, cross-hatched fringe pattern. Very fine interferometric fringes appear to be more easily identified against such a background than against the speckle pattern produced by a typical etched glass diffuser. No dramatic improvement, however, is noted over the use of a quality opal glass diffuser.

It should be noted that these results are of a rather preliminary nature. The subject may be pursued further.

6.3. MULTIDIRECTIONAL ILLUMINATION

A very simple, yet potentially useful, application of crossed gratings is to decompose an illuminating plane wave into a set of plane waves of various discrete spatial frequencies. When a crossed grating is inserted between a collimating lens and the transparent object to be studied, the object is, in effect, illuminated by several plane waves, each traveling from a different direction. An interferogram of the object thus illuminated produced in the usual manner can be thought of as consisting of several interferograms—one produced by each of the plane waves. These interferograms can easily be separated by passing the output of the hologram through a spherical lens. This is equivalent to taking a spatial Fourier transform of the hologram output. By placing a small aperture in the focal plane of the lens one can block out all but one of the component plane waves. After passing this filtered output through a second lens one obtains a single plane-wave produced interferogram. This interferogram is free of laser speckle.

By this method a transparent object may be interferometrically studied from a finite number of directions using a single hologram. No laser speckle degrades the fringe pattern. It is interesting to note that the fringe interpretation of interferograms produced with diffuse illumination [1] shows that the pattern observed is always equivalent, to a first approximation, to that of an interferogram produced by a plane wave traveling in the viewing direction. Hence, for quantitative interpretation purposes the crossed grating illumination provides the same type of information as the diffuse illumination; however, the problems of speckle are eliminated at the expense of limiting the number of available viewing directions.

Preliminary experiments indicate that this method is readily applied to small objects. We hope to carry out a more detailed experimental investigation of this method in the near future.

7

MODULATED REFERENCE-WAVE HOLOGRAPHY

Modulated reference-wave holography (MRWH) is a generalized time-average holographic technique that was described in the previous report [1]. In essence, any time-average holographic technique depends on the fact that the object light becomes modulated by the vibrating object and that the hologram acts as a narrowband filter applied to this light. This filtering action is dramatically displayed as a set of fringes on the reconstructed object. In MRWH we modulate the reference wave in a known way. The hologram now acts as a filter applied to the cross-correlation between the object-wave spectrum and the reference-wave spectrum. The very nature of the fringes on the reconstructed object can now be controlled by controlling the reference-wave modulation.

In the previous report we demonstrated that sinusoidal phase modulation of the reference wave will give the relative phases of the vibration of the object as well as their amplitudes. With SSSC (single-sideband suppressed-carrier) modulation of the reference wave we found that we had optical heterodyne detection for small vibrations of the object. Since then we have looked at other types of reference-wave modulation and have used the technique on diffusely reflective objects as well as transparent ones.

In normal time-average holography, large amplitude vibrations produce such fine fringes on the reconstruction that it is almost impossible to use the fringes for measurements. It has been found that MRWH can be used to advantage for large amplitude vibrations. As an example, we will demonstrate that SSSC modulation can decrease the number of fringes. The technique is based on the fact that if the single-sideband frequency of the reference wave (for SSSC modulation) is equal to n^{th} order sideband of the object wave, then the intensity of the reconstruction (i.e., the fringe variation on the image) is proportional to $J_n^2(M)$ where $J_n(M)$ is the n^{th} order Bessel function with argument $M = \frac{4\pi}{\lambda} A$. Here A is amplitude of vibration and λ the wavelength of the laser light. The initial maximum of the Bessel function (i.e., the brightest band in the reconstruction) occurs for larger and larger values of the argument as the order of the Bessel function increases. Hence any number of fringes, corresponding to the smaller vibration amplitudes, can be eliminated by working with a higher order Bessel function.

This effect is illustrated in Fig. 22. The object is a small (about 3 in. in diameter) loudspeaker driven at about 1 kHz. Figure 22a shows a normal time-average (i.e., the zeroth order SSSC) hologram for this speaker. The reconstruction is proportional to $J_0^2(M)$. If the speaker is driven much harder, the fringes become too fine to see with the eye. For illustrative and comparative purposes we have limited our drive amplitude. However, we still

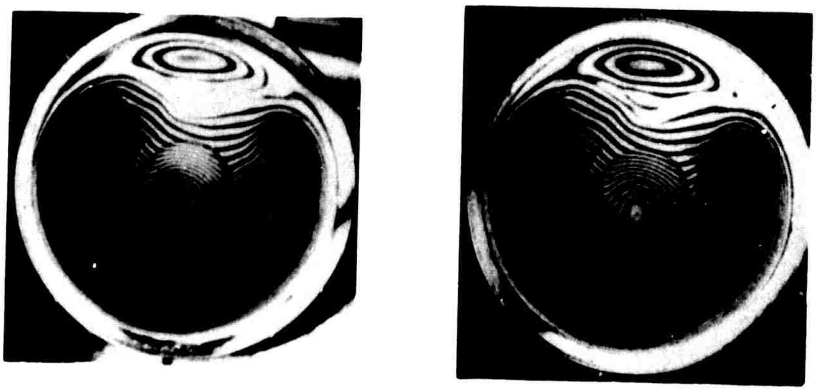

(a) The 0th Order (normal time-average hologram).

(b) The 1st Order

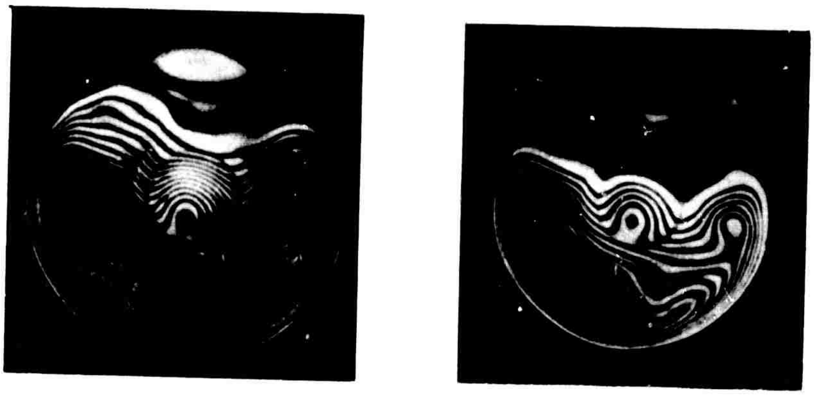

(c) The 9th Order

(d) The 28th Order

FIGURE 22. MODULATED REFERENCE-WAVE HOLOGRAPHY OF A VIBRATING LOUDSPEAKER. The reference-wave modulation is of the single-sideband suppressed-carrier type.

have one difficulty that is very common with normal time-average holography. The dynamic range of the fringe is so great that it is difficult, if not impossible, to make a proper exposure of all the fringes. This problem is also alleviated with higher order sideband holography. Figures 22b, c, and d show the 1st, 9th, and 28th order sideband cases, respectively [and the location of fringes given by $J_1^2(M)$, $J_9^2(M)$, and $J_{28}^2(M)$, respectively]. As all the figures show, the speaker vibrates, not as a piston, but in two separate peaks. Knowing the properties of $J_9^2(M)$, we see that the smaller peak is at about $1\lambda = 0.63\ \mu m$ of amplitude. From $J_{28}(M)$ the center of the cone is seen to have an amplitude at about $3\lambda = 1.9\ \mu m$. Although these same results can be obtained from Fig. 22a, it is becoming difficult to count the number of fringes from a vibration null. As a matter of fact, it is difficult to be sure where the nulls are. It is more convenient to look at the first peak of a higher order Bessel function and count, if necessary, only a few fringes with no ambiguity.

Other MRWH techniques are under investigation and are being considered for application to this contract.

8
FLAW DETECTION BY HOLOGRAM INTERFEROMETRY

8.1. INTRODUCTION

During this first year of the ARPA holographic nondestructive testing program, a substantial amount of investigation has been done. The first semiannual report [1] described our initial efforts to find a suitable test specimen for holographic nondestructive testing. This early study resulted in a qualitative description of the cylindrical specimen we had chosen and of the problems associated with testing it. Based upon this initial program, then, the second phase of experimentation began and is the subject of this report.

8.2. PNEUMATIC TECHNIQUE

The first method of stressing the test cylinder, as outlined in the previous report, consists of expanding it radially by increasing the internal air pressure to approximately 30 psi. The radial expansion of the cylinder is proportional to this applied air pressure. Holographic interferometry then reveals this expansional information in the form of interference fringes. Nonuniformities in expansion due to specimen flaws cause a corresponding nonuniformity of interference fringes which are used to locate the defects.

Early experimentation with the pneumatic technique showed that the full use of our maximum testing stress of 70 psi could not be utilized because it caused gross expansional motion of the cylinder. Since only differential motion contains useful information, we decided that viewing the cylinder from below as shown in Fig. 23 would be most appropriate. It is clear that the smallest gross expansional motion is in the direction of sensitivity vector $\vec{S}_2$ and not $\vec{S}_1$. Hence, a mirror was placed 45° to the horizontal below the cylinder (Fig. 24) for the purpose of illumination and viewing the bottom surface. We found this technique to be extremely effective in eliminating irrelevant motion.

In order to obtain a quantitative correlation between the stressing function and flaw detection, it was necessary to program a set of well defined defects into the test cylinder. This was done by impressing a one-inch-diameter steel ball into the outside face of the cylinder and then measuring the depth of the resulting indentation. Using this method, two sets of six dimples each were programmed. The specifications are listed in Table 4.

To date, the pneumatic experiments have been the most successful. Nine of the twelve programmed flaws were detected using this technique. A similar experiment which yielded almost identical results consisted of evacuating the cylindrical chamber, thereby using atmospheric pressure to stress the object. With a maximum vacuum of 30-in. Hg, eight of the twelve dimples were seen. Photographs of holograms that reveal these flaws can be seen in Figs. 25 and 26.

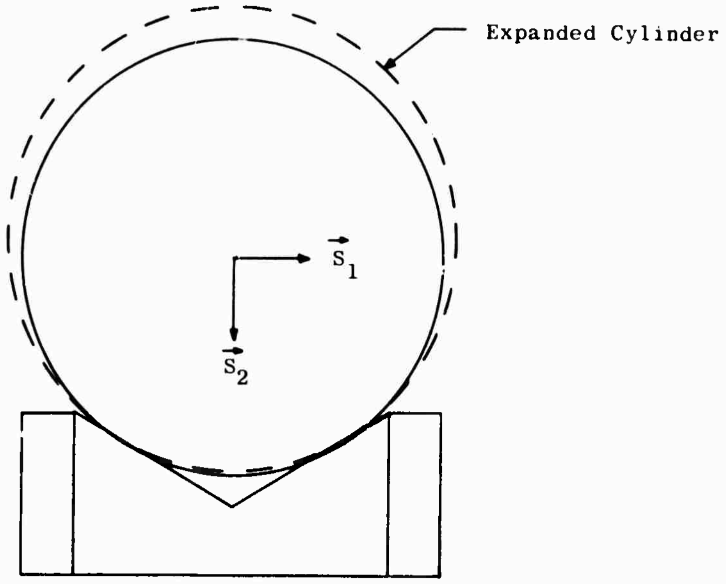

FIGURE 23. EXPANSION OF TEST CYLINDER IN THE DIRECTION OF SENSITIVITY VECTORS $\bar{S}_1$ AND $\bar{S}_2$

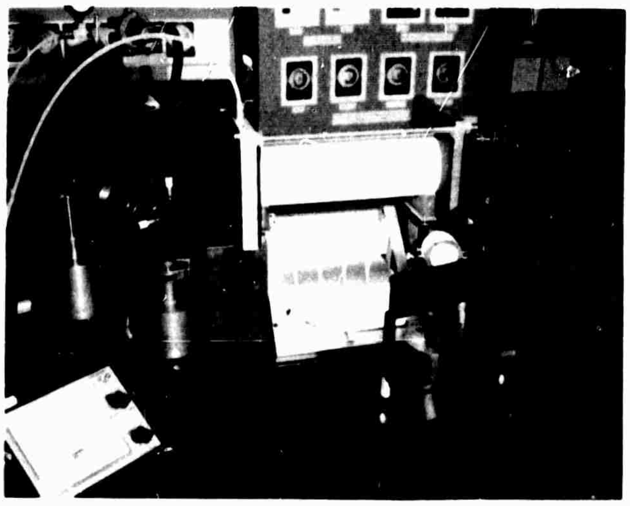

FIGURE 24. HOLOGRAM APPARATUS FOR PNEUMATIC TESTING

TABLE 4. PROGRAM OF FLAWS

Flaw	Side	Depth (in.)	Successful Technique	Applied Technique
1	A	0.037	P E	P E H V
2	A	0.027	P E	P E H V
3	A	0.022	P E H	P E H V
4	A	0.018	P E H	P E H V
5	A	0.013	P E	P E H V
6	A	0.004		P E H V
7	B	0.002		P E H C V
8	B	0.015	P E C	P E H C V
9	B	0.005	P	P E H C V
10	B	0.007	E	P E H C V
11	B	0.010	P E	P E H C V
12	B	0.020	P C	P E H C V

Technique Code: P = pneumatic
E = evacuation by vacuum
H = heat
C = compression
V = vibration

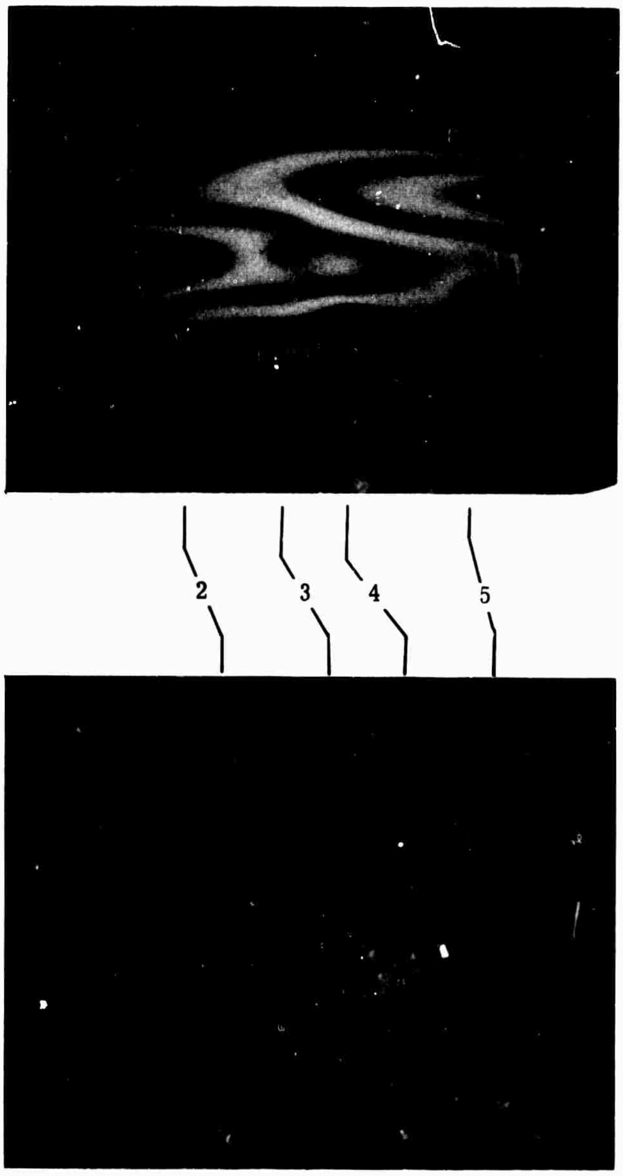

(a) Pneumatic Technique at
30 psi Reveals Flaws 2, 3, 4, 5

(b) Vacuum Technique of
Same Area, 30-in Hg

FIGURE 25. DOUBLE EXPOSURE INTERFEROGRAM

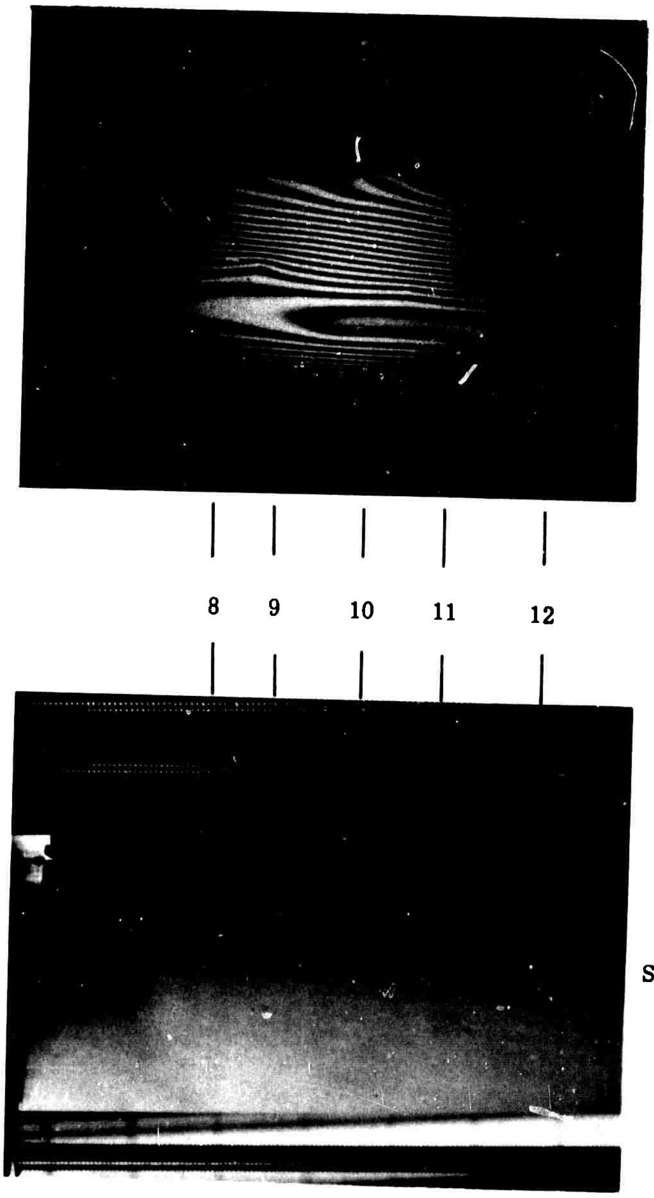

(a) Double Exposure
Interferogram Reveals
Flaws 8, 9, 11, 12

(b) White Light Photograph
of Test Specimen Reproduced to
Same Scale as (a) for Flaw Reference

FIGURE 26. FLAW DETECTION USING VACUUM TECHNIQUE

Three other techniques have been used in an attempt to reveal increasingly smaller flaws. These techniques are: (1) thermal stress, (2) compressive axial loading, and (3) vibrational excitation. A short description of these experiments, their justification, and the results follows.

8.3. THERMAL TECHNIQUE

If a thermal gradient exists across a uniform surface, it should cause a corresponding displacement gradient to form. If, on the other hand, an anomaly existed on the surface, the thermal expansion characteristics may differ enough from the surrounding area to disturb the previously well-behaved strain pattern. With this in mind, we attempted to reveal the programmed flaw by heating the cylinder with an approximate point source (photoflood lamp) located within the cylindrical interior. The first exposure of the hologram plate was taken before the heat was applied. The second exposure was taken after the heat source had been on for 10 seconds and allowed to cool for 10 seconds. Long exposure times (8 seconds) required stability of fringe patterns, which in turn required a cooling-off period before the second exposure.

The interference fringe pattern that resulted can be seen in Fig. 27. Although two of the flaws can be seen as small perturbations in the regular fringe pattern, the thermal technique is not as effective as we had hoped, and is definitely inferior to pneumatic stressing. Also, the position of the heat source along the axis determined which flaws could be revealed, even though the thermal gradient existed across the bulk of the cylinder regardless of heat source position.

8.4. COMPRESSION TECHNIQUE

When an object such as our test cylinder is put into axial compression, its length will tend to decrease and there will be radial and tangential expansion. Because of the symmetry of the cylinder, one would expect uniform (or at least smoothly varying) strain across its entire surface. If, however, there is a disruption of symmetry by a dimple, it could be expected that the uniformity of expansion would be perturbed.

Figure 28 shows the experimental apparatus used. A hydraulic press capable of delivering up to 20,000 lb. of axial compression was used to stress the cylinder. The double exposure technique consisted of exposing first with a small (100 lb.) load and then again with a large load, with the relative difference in force being the relevant quantity. In Fig. 29, the interferogram resulting from a compression loading experiment is seen. Note that two of the programmed flaws did cause severe distortion of the fringe pattern.

An important result of this experiment not related to the detection of the programmed flaws but significant to general nondestructive testing is the interferometric fringe pattern

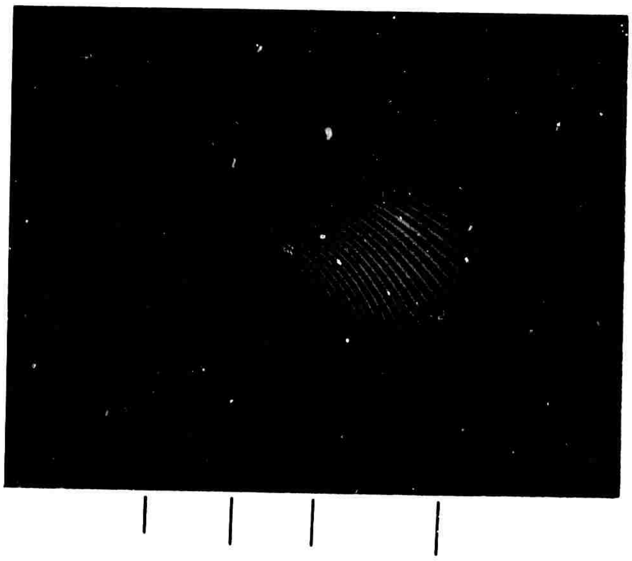

(a) Double Exposure Interferogram Using Thermal Technique Reveals Flaws 3 and 4

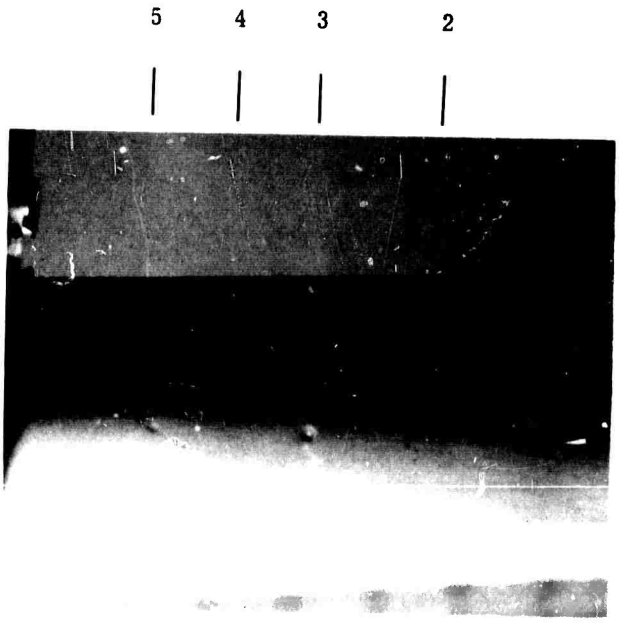

(b) Photograph of Test Specimen for Flaw Reference

FIGURE 27. FLAW DETECTION USING THERMAL TECHNIQUE

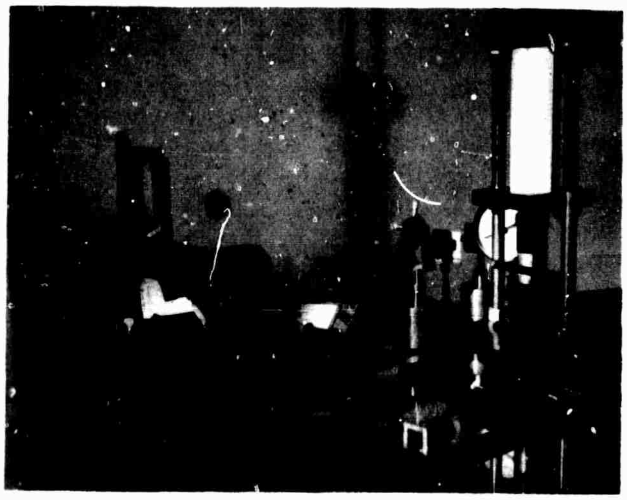

FIGURE 28. APPARATUS FOR AXIAL COMPRESSION EXPERIMENTS

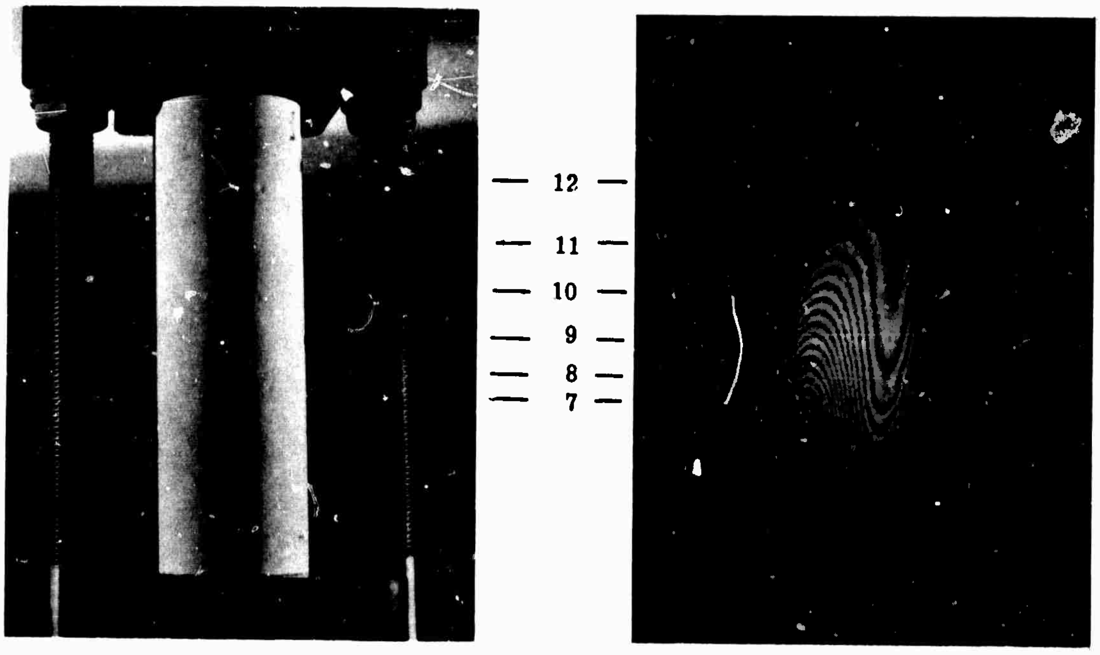

(a) Photograph of Test Specimen for Flaw Reference

(b) Double Exposure Interferogram Using Axial Load of 750 lb Reveals Flaws 8 and 12

FIGURE 29. FLAW DETECTION USING COMPRESSION TECHNIQUE

produced over the entire cylindrical surface. Here, in one glance, can be seen the whole strain pattern for the hemi-cylinder. One can see, for instance, the local minima (or maxima) of strain in the lower left and the accompanying large strain gradient surrounding it. It can also be seen that there is almost no difference in the displacement between the two flaws (8 and 12) that are visible. In other words, flaws 8 and 12, and all points on the line segment connecting them, moved approximately the same amount. Note that the boundary effects are also available for analysis, and have been obtained in what may be the most convenient and most accurate method available.

8.5. VIBRATION TECHNIQUE

A great deal of analysis of vibrational modes in cylinders has been done at Cooley Electronics Laboratory in connection with other contracts. As a result, the time-average holographic interferometric patterns of a sinusoidally vibrating cylinder in resonance and with clamped ends are familiar and well understood. For this case, the radial displacement can be exactly described as

$$\Delta r = A \sin \frac{m\pi x}{L} \cos n\theta \cos \omega t$$

where A = Peak displacement amplitude
x = Distance from one end of cylinder
θ = Circumferential angle measured counterclockwise from a radial antinode
ω = Angular vibration frequency
m = Number of axial half wavelengths of vibration
n = Number of circumferential full wavelengths of vibration

(Note: $m = 1$, $n = 2$ for interferogram of Fig. 30.)

This expression for radial movement is derived for an ideal cylinder with all its associated symmetry. The fringe patterns that result from this motion should be thought of as contour lines that depict points of constant vibrational amplitude in the direction of the sensitivity vector. Each successive fringe marks a difference in projected motion of approximately $\lambda/2$. More exactly, the spacing between each fringe and the total intensity pattern over the hologram is described by the squared, zero-order Bessel function of the first kind [16]. With this background, then, it was reasoned that any departure from the cylinder's natural symmetry due to programmed defects would result in irregularities in the vibrational displacements predicted, and hence in the fringe patterns observed.

Two series of experiments were conducted. The first was with the cylinder experiencing 1000 lb. of axial compression and the second was with only enough compression to clamp the ends securely. The cylinder was then excited by a magnetic transducer which was driven by

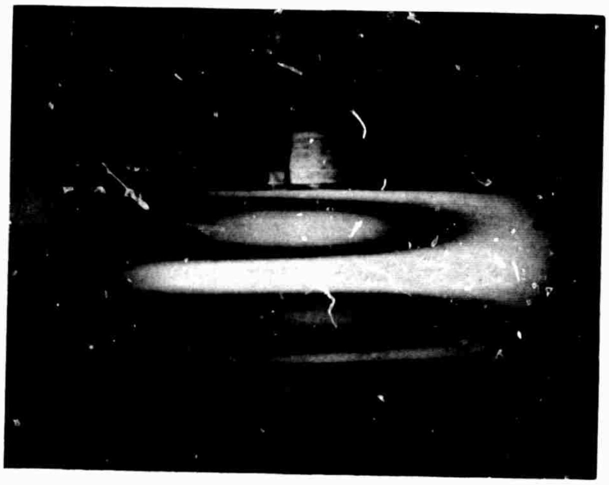

(a) Time-Averaged Interferogram of Cylinder; Mechanical Vibratory Frequency is 3012 Hz

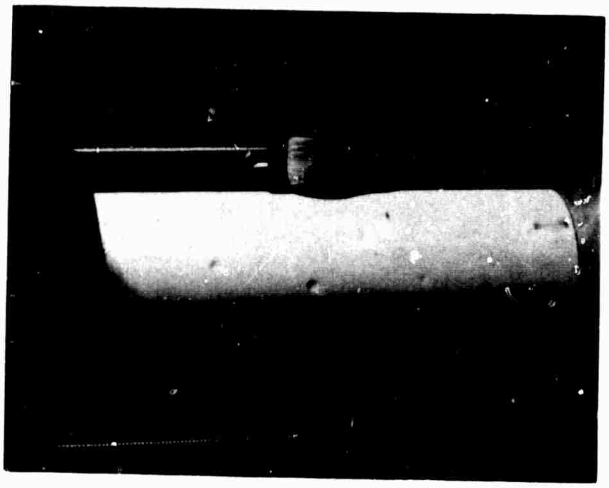

(b) Photograph of Cylinder

FIGURE 30. VIBRATION TECHNIQUE

an amplifier and sine wave generator. Resonances were found by observing real-time holograms as excitation frequency and amplitude were varied. As seen in Fig. 30, the degree of asymmetry introduced by the dimples was not nearly enough to affect the theoretically predicted vibrational patterns and hence no flaws were revealed using this technique. Figure 31 shows the experimental apparatus used for vibration analysis.

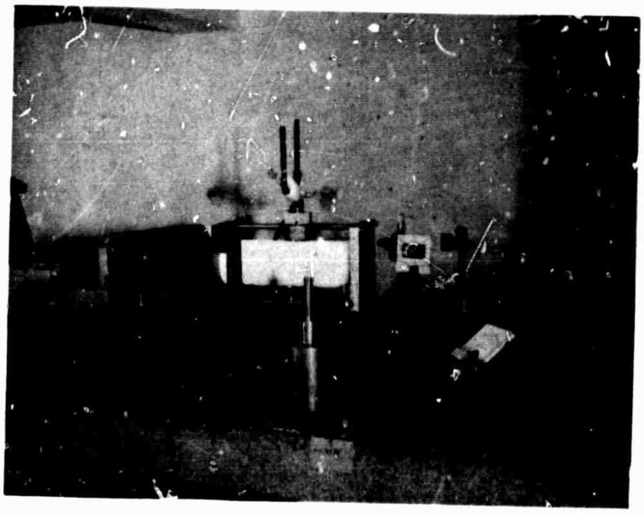

FIGURE 31. EXPERIMENTAL APPARATUS FOR VIBRATION ANALYSIS

9
ULTRASONIC HOLOGRAPHY

Because of our great involvement with the optical investigation discussed in this report, and because of personnel changes in the laboratory, no experimentation in ultrasonic holography has been conducted during this period. Within the past month, however, one member of our research staff has been assigned the task of studying new areas of meaningful investigation in this field and suggesting a program for future work in ultrasonic holography.

Appendix I
STRESS CORROSION CRACKING OF TITANIUM ALLOYS

Kiefer and Harple [17], the first to study the stress corrosion cracking (SCC) of commercially pure titanium after the material became of general industrial interest, found that SCC occurred in red fuming nitric acid. Rittenhouse [18] later extended this work and established limits on the NO_2 and H_2O content in the acid which inhibited the cracking.

It was generally believed that titanium alloys were basically free from SCC in other common environments until SCC was encountered when unprotected titanium alloys were exposed to halogenated atmospheres, particularly NaCl. Brown [19] studied SCC in synthetic and natural sea water at room temperature in the presence of a flaw or stress concentration. Lane and co-workers [20] found that the attack was a function of the aluminum content and heat treatment. They showed SCC could be reduced by lowering aluminum content or by adding molybdenum or vanadium alloying elements.

The SCC of titanium alloys exposed to chloride salts at elevated temperatures has been of more general concern, however, since titanium has been proposed as a material for supersonic transport aircraft which will experience high temperatures, possibly in a chloride environment. Logan [21] and Heimerl and co-workers [22] studied SCC of Ti-8Al-1Mo-1V at temperatures from 400 to 750°F in controlled NaCl environments. Both reports indicate that there would be no cracking without oxygen present.

Stress corrosion cracking of titanium alloys in bromide-methanol solutions has been reported by Cocks and co-workers [23] who studied SCC of Ti-6Al-4V. Sedriks and co-workers [24] reported SCC in iodine-methanol solutions. Sedriks found that corrosion susceptibility increased with increasing aluminum content.

Cracking in dry reagent grade methanol has recently been of interest, since titanium is used in methanol storage tanks and methanol is used as a test fluid to test the integrity of spacecraft fuel tanks [25]. O'Brien [26] and Herigen [27] both reported SCC of Ti-6Al-8V stressed in dry reagent methanol. Haney [28], however, was unable to get failure in pure methanol and believes that contaminates of chloride present in the methanol may have caused the SCC in previous experiments. He reported concentrations of 10^{-5}N. HCl caused SCC in Ti-13V-11A-3Al, but no failures were obtained using "pure" methanol.

Recently, Crimmins and Green [29] used a new nondestructive acoustic emission technique to monitor the SCC process of a notched specimen of Ti-6Al-4V in reagent grade methanol. Their data gave a definite indication of pop-in, followed by an increased rate of stress wave emission until failure.

The history of titanium SCC given is intended as a short review; for a more complete study and additional references, the reader may refer to Refs. [21], [26], or [30].

Appendix II
THEORY OF AUTOMATIC REFERENCE BEAM COMPENSATION

Let us assume that we are recording an image plane hologram with two frequencies and a separate plane wave reference beam for each frequency.

The reconstruction beam can be of some third frequency and can be from a point source. The reconstructed wavefronts in the hologram plane are:

$$S_1 + S_2 = e^{jk_3\overline{r_3}}\left[e^{jk_1(r_0+r_1-r_{21})} + e^{jk_2(r_0+r_1-r_{22})}\right]$$

$$|S_1 + S_2|^2 = \left\{e^{j\Delta k(r_0+r_1)}e^{j[k_2(r_{22}-r_{21})k_1]}\right.$$

$$\left. 2 + e^{-j\Delta k(r_0+r_1)}e^{-j[k_2(r_{22}-r_{21})k_1]}\right\}$$

where $k_i = 2\pi/\lambda_i$, $\Delta k = k_2 - k_1$, $r_0 + r_1$ is the distance between the object illumination point and a given hologram point via the corresponding object point, and r_{21} and r_{22} are the distances to the two different reference points from the hologram point. Hence

$$|S_1 + S_2|^2 = 2 + 2\cos\left[\Delta k(r_0 + r_1) + (k_2r_{22} - k_1r_{21})\right]$$

In order to have error-free contouring, we require

$$k_2r_{22} - k_1r_{21} \neq f(x)$$

where x represents any hologram plane coordinate. For plane wave reference beams striking the hologram plane, we have the following x phase variation

$$k_2r_{22} = \frac{2\pi}{\lambda_2}\sin\theta_2 x + K_2$$

$$k_1r_{21} = \frac{2\pi}{\lambda_1}\sin\theta_1 x + K_1$$

Obviously, the condition given below

$$\frac{\sin\theta_1}{\lambda_1} = \frac{\sin\theta_2}{\lambda_2}$$

results in

$$k_2r_{22} - k_1r_{21} = K_2 - K_1 \neq f(x)$$

Suppose we have tried to satisfy the above condition by some reference beam compensation technique. How much error is allowable? A very strict requirement would be

$$\left|\frac{2\pi}{\lambda_2}\sin\theta_{2X} - \frac{2\pi}{\lambda_1}\sin\theta_{1X}\right| < \frac{\pi}{4}$$

where $X = |x_{max} - x_{min}|$ for the image. This becomes

$$\left|\frac{\sin\theta_2}{\lambda_2} - \frac{\sin\theta_1}{\lambda_1}\right| < \frac{1}{8X}$$

Now let $\theta_2 = \theta_{2p} + \epsilon$ where θ_{2p} represents the error-free offset angle given θ_1, λ_1, and λ_2

$$\frac{\sin\theta_{2p}}{\lambda_2} = \frac{\sin\theta_1}{\lambda_1}$$

Then we have

$$\left|\frac{\sin\theta_{2p}\cos\epsilon + \sin\epsilon\cos\theta_{2p}}{\lambda_2} - \frac{\sin\theta_1}{\lambda_1}\right| < \frac{1}{8X}$$

We can set $\cos\epsilon = 1$ and $\sin\epsilon = \epsilon$ as a reasonable approximation for small ϵ:

$$\left|\frac{\epsilon\cos\theta_{2p}}{\lambda_2}\right| < \frac{1}{8X} + \left(\frac{\cos\epsilon}{\lambda_1} - \frac{1}{\lambda_1}\right)\sin\theta_1$$

$$|\epsilon| < \frac{\lambda_2}{8X\,|\cos\theta_{2p}|} = \frac{\lambda_1}{8X\,|\cos\theta_{1p}|}$$

Apparently, the allowable error increases as θ_{2p} increases. However, it could be that the probable error increases with θ_{2p} as well. This will be examined in the future.

We can see that the above constraint on $|\epsilon|$ is quite severe by the following order of magnitude calculation

$\lambda \sim 1 \times 10^{-6}$ meter

$X \sim 1 \times 10^{-2}$ meter

$\cos\theta_{2p} \sim 1$

$|\epsilon| \sim 1 \times 10^{-5} \sim 2$ seconds of arc

This constraint on $|\epsilon|$ is severe, but within the state of the art in optical alignment techniques.

We have been discussing the direct effect of $|\epsilon|$ on the errors in the contour map, and we will investigate the possibility of putting a reference surface near the object so that we would be able to subtract out the systematic portion of the error in reference beam compensation. But now we would like to turn our attention to the effect of $|\epsilon|$ on fringe visibility.

For those object points whose images are well focused in the hologram plane, the contour fringe visibility should be affected only by the overall resolution of the optical system used. For all other points, the image point-pairs do not coincide exactly and, as the point-pairs become resolvable, the fringe visibility begins to fall off. In Section 4, relationships were derived between resolution, contouring interval, maximum longitudinal extent and maximum slope. These relationshops yielded definite constraints which have to be met if fringe visibility is to exceed a given standard. We would now like to know how these constraints are affected by errors in reference-beam compensation, and how we can express these relationships from a point of view other than the interference between two coherent images. These questions will be considered later.

Figure 32 depicts two coherent aerial images centered longitudinally on the hologram plane. Let us assume that due to ϵ, an angle δ exists between the centroids of the two different light bundles forming images of a given object point. Let the image points be at a maximum distance Z from the hologram plane. Then the image point displacements are

$$(\Delta z)_{max} = \frac{\Delta\lambda}{\lambda} Z$$

$$(\Delta x)_{max} = \delta Z$$

Now, δ will be of the same order of magnitude as ϵ, so let us conservatively state

$$\delta \sim \frac{\lambda}{X}$$

$$(\Delta x)_{max} = \frac{\lambda}{X} Z$$

In order to have good fringe visibility, the following condition must be satisfied

$$(\Delta x)_{max} < \rho = \lambda F$$

But since we typically have

$$F >> 1$$

and

$$\frac{Z}{X} << 1$$

it seems obvious that δ will never have any significant effect on fringe visibility.

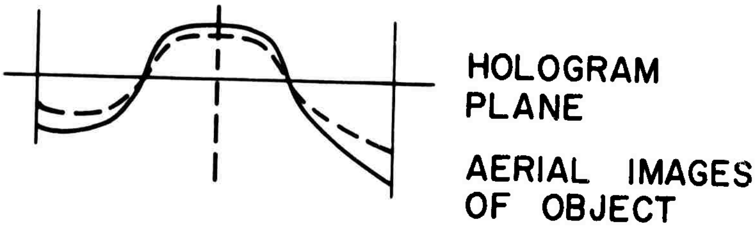

(a) Representation of Two Different Aerial Images of the Object Near the Hologram Plane

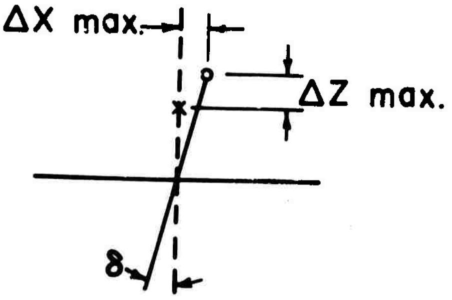

(b) Expanded Drawing of a Typical Image-Point Pair

FIGURE 32. AERIAL IMAGES IN HOLOGRAM PLANE

REFERENCES

1. E. N. Leith, et.al., Investigation of Holographic Testing Techniques, Report No. 2420-5-P, Willow Run Laboratories of the Institute of Science and Technology, The University of Michigan, Ann Arbor, August 1969.
2. A. A. Friesem and C. M. Vest, Detection of Micro Fractures by Holographic Interferometry, Appl. Optics, Vol. 8, pp. 1253-54, 1969.
3. C. M. Vest, E. L. McKague, Jr., and A. A. Friesem, Holographic Detection of Microcracks, submitted for publication.
4. T. D. Dudderar, Applications of Holography to Fracture Mechanics, Experimental Mechs., Vol. 9, p. 281, 1969.
5. C. A. W. Peterson and R. R. Vandervoort, Stress-Cracking in the Uranium-10 Without Molybdenum Alloy, Report No. UCRL-7767, Lawrence Radiation Laboratory of The University of California, Livermore, California, March 1964.
6. R. M. Grant and G. M. Brown, Holographic Nondestructive Testing (HNDT), Materials Evaluation, Vol. 27, p. 79, April 1969.
7. K. A. Haines and B. P. Hildebrand, Surface Deformation Measurements Using the Wavefront Reconstruction Technique, Appl. Optics, Vol. 5, p. 595, 1966.
8. B. P. Hildebrand, A General Analysis of Contour Holography, Doctoral Dissertation, The University of Michigan, 1967.
9. J. R. Varner and J. S. Zelenka, A New Method for Generating Depth Contours Holographically, Appl. Optics, Vol. 7, p. 2107, 1968.
10. O. Bryngdahl and A. W. Lohmann, Interferograms are Image Holograms, J.O.S.A., Vol. 58, p. 141, 1968.
11. Tsuruta, et.al., Japan J. Appl. Physics, Vol. 6, p. 661, 1967.
12. J. R. Varner and J. S. Zelenka, Multiple-Index Holographic Contouring, Appl. Optics, Vol. 8, p. 1431, 1969.
13. L. I. Goldfisher, Autocorrelation Function and Power Spectral Density of Laser-Produced Speckle Patterns, J.O.S.A., Vol. 55, p. 247, March 1965.
14. L. H. Tanner, A Study of Fringe Clarity in Laser Interferometry and Holography, J. Sci. Instruments, Vol. 1, p. 517, 1968.
15. E. N. Leith and J. Upatnieks, Imaging with Pseudo-Randomly Diffused Coherent Illumination, Appl. Optics, Vol. 7, p. 2085, October 1968.
16. R. L. Powell and K. A. Stetson, Interferometric Vibration Analysis by Wavefront Reconstruction, J.O.S.A., Vol. 55, p. 1593, December 1965.
17. G. C. Kiefer and W. W. Harple, Stress Corrosion Cracking of Commercially Pure Titanium, Metal Progress, Vol. 63, pp. 74-76, 1953.
18. J. B. Rittenhouse, Corrosion, Pyrophoricity, and Stress Corrosion Cracking of Titanium Alloys in Fuming Nitric Acid, Trans. ASM, Vol. 51, pp. 871-895, 1959.
19. B. F. Brown, New Stress-Corrosion Cracking Test for High-Strength Alloys, Materials Research and Standards, No. 3, pp. 129-133, 1966.

20. I. R. Lane, J. L. Cavallars, and A.G.S. Morton, Sea-Water Embrittlement of Titanium, Stress-Corrosion Cracking of Titanium, ASTM, STP 397, pp. 246-257, 1966.
21. H. L. Logan and others, Chemical and Physical Mechanisms of Salt Stress-Corrosion Cracking in the Titanium 8-1-1 Alloy, Stress-Corrosion Cracking of Titanium, ASTM, STP 397, pp. 215-229, 1966.
22. G. J. Heimerl and others, Salt Stress Corrosion of Ti-8 Al-1Mo-1V Alloy at Elevated Temperatures, Stress-Corrosion Cracking of Titanium, ASTM, STP 397, pp. 194-214, 1966.
23. F. H. Cocks, J. F. Russo, and S. B. Brumner, The Separation of Corrosion and Stress Effects in Stress Corrosion: Ti-6Al-4V in Bromine-Methanol Solutions, Corrosion, Vol. 24, pp. 206-208, 1968.
24. A. J. Sedriks, J. A. S. Green, and P. W. Slattery, Stress Corrosion Cracking and Corrosion Behavior of Ti and Ti-Al Alloys in Methanol Iodine Solutions, Corrosion, Vol. 24, pp. 172-177, 1968.
25. R. E. Johnson, NASA Experiences with Ti-6Al-1V in Methanol, Accelerated Crack Propagation of Titanium by Methanol, Halogenated Hydrocarbons, and Other Solutions, DMIC Memorandum 228, pp. 2-7, 1967.
26. R. O'Brien, Premature Environmental Stress Cracking of Titanium in Methanol, Freon, and Other Solutions, Accelerated Crack Propagation of Titanium by Methanol, Halogenated Hydrocarbons, and Other Solutions, DMIC Memorandum 228, pp. 8-9, 1967.
27. H. R. Herrigel, Titanium N-Bends in Organic Liquids, Effect of Inhibitors, Accelerated Crack Propagation of Titanium by Methanol, Halogenated Hydrocarbons, and Other Solutions, DMIC Memorandum 228, pp. 16-19, 1967.
28. E. G. Haney and W. R. Wearmouth, Effect of "Pure" Methanol on the Cracking of Titanium, Corrosion Science, Vol. 25, pp. 87-91, 1969.
29. P. P. Crimmins and A. T. Green, Development of a Nondestructive Testing Technique to Determine Flaw Criticality, ARPA Number 1244, Program Code 8D10, February 1969.
30. H. L. Logan, The Stress Corrosion of Metals, Wiley & Sons, pp. 238-251, 1968.

Unclassified
Security Classification

DOCUMENT CONTROL DATA - R & D

(Security classification of title, body of abstract and indexing annotation must be entered when the overall report is classified)

1. ORIGINATING ACTIVITY *(Corporate author)* Willow Run Laboratories of the Institute of Science and Technology, The University of Michigan, Ann Arbor	2a. REPORT SECURITY CLASSIFICATION UNCLASSIFIED
	2b. GROUP

3. REPORT TITLE
INVESTIGATION OF HOLOGRAPHIC TESTING TECHNIQUES

4. DESCRIPTIVE NOTES *(Type of report and inclusive dates)*
Semiannual Report, 1 June Through 30 November 1969

5. AUTHOR(S) *(First name, middle initial, last name)*
Emmett N. Leith
Charles M. Vest

6. REPORT DATE April 1970	7a. TOTAL NO. OF PAGES x + 64	7b. NO. OF REFS 30

8a. CONTRACT OR GRANT NO. DAAG46-69-C-0017	9a. ORIGINATOR'S REPORT NUMBER(S) 2420-9-P
b. PROJECT NO. ARPA Order No. 1245	
c. Program Code No. 8D10	9b. OTHER REPORT NO(S) *(Any other numbers that may be assigned this report)*
d.	

10. DISTRIBUTION STATEMENT

11. SUPPLEMENTARY NOTES	12. SPONSORING MILITARY ACTIVITY Advanced Research Projects Agency Department of Defense Washington, D. C.

13. ABSTRACT

This second semiannual report includes studies of interferometric detection of stress corrosion cracking, testing of honeycomb sandwich structures, techniques developed for pulsed-laser contouring and interferometry, laser speckle reduction in interferometry, modulated reference-wave holography, and flaw detection.

Holographic interferometry has been used to detect initiation of stress corrosion, monitor the progressing of delayed cracking, and detect bond defects in an aircraft trim tab of honeycomb structure.

The several theoretical and experimental investigations conducted include the development of multiple-wavelength holographic interferometry, the study of techniques for improving interferometry of three-dimensional transparent objects, the application of modulated reference-wave holography to vibrating diffusely reflecting objects, and the application of hologram interferometry to detection of flaws in cylindrical steel objects.

14 KEY WORDS	LINK A		LINK B		LINK C	
	ROLE	WT	ROLE	WT	ROLE	WT
Holographic testing						
Stress corrosion cracking						
Interferometry						
Pulsed-laser holography						
Nondestructive testing						
Multiple-wavelength holography						